THE ASTROPHYSICAL JOURNAL, 529:886–910, 2000 February 1

THE ASYMMETRY OF GALAXIES: PHYSICAL MORPHOLOGY FOR NEARBY AND HIGH-REDSHIFT GALAXIES

CHRISTOPHER J. CONSELICE AND MATTHEW A. BERSHADY
Department of Astronomy, University of Wisconsin, Madison, 475 North Charter Street, Madison, WI 53706-1582;
chris@astro.wisc.edu; mab@astro.wisc.edu

AND

ANNA JANGREN
Department of Astronomy and Astrophysics, Pennsylvania State University, 525 Davey Lab, University Park, PA 16802;
jangren@astro.psu.edu
Received 1999 May 7; accepted 1999 August 23

ABSTRACT

We present a detailed study of rotational asymmetry in galaxies for both morphological and physical diagnostic purposes. An unambiguous method for computing asymmetry is developed, which is robust for both distant and nearby galaxies. By degrading real galaxy images, we test the reliability of this asymmetry measure over a range of observational conditions, e.g., spatial resolution and signal-to-noise ratio (S/N). Compared to previous methods, this new algorithm avoids the ambiguity associated with choosing a center by using a minimization method and successfully corrects for variations in S/N. There is, however, a strong relationship between the rotational asymmetry and physical resolution (distance at fixed spatial resolution): objects become more symmetric when less well-resolved. We further investigate asymmetry as a function of galactic radius and rotation. We find the asymmetry index has a strong radial dependence that differs vastly between Hubble types. As a result, a meaningful asymmetry index must be specified within a well-defined radius representative of the physical galaxy scale. We enumerate several viable alternatives, which exclude the use of isophotes. Asymmetry as a function of angle (A_ϕ) is also a useful indicator of ellipticity and higher order azimuthal structure. In general, we show that the power of asymmetry as a morphological parameter lies in the strong correlation with $B-V$ color for galaxies undergoing normal star formation spanning all Hubble types from ellipticals to irregular galaxies. The few interacting galaxies in our study do not fall on this asymmetry-color "fiducial sequence," as these galaxies are too asymmetric for their color. We suggest this fact can be used to distinguish between "normal" galaxies and galaxies undergoing an interaction or merger.

Subject headings: galaxies: photometry — galaxies: structure

1. INTRODUCTION

1.1. *Galaxy Morphology*

Ever since galaxies were recognized as distinct physical systems, one of the main goals in extragalactic astronomy has been to characterize their forms, or morphology, and to determine how this classification relates to physical properties. This basic taxonomical process is indeed the basis for any observational science. The first attempts at classification were on a subjective level and began with the work of Curtis (1918), Hubble (1926, 1936), and Sandage (1961). As more images of galaxies became available, the morphological system developed by Hubble was generally adopted by all astronomers and later refined by van den Bergh (1960a, 1960b) and de Vaucouleurs (1959). Other morphological systems were also developed by Morgan (1958) based on the correlation of the physical characteristics of galaxy spectra with the concentration of the light profiles. Yet, since the time of Hubble's 1926 work, the system of morphology for galaxies has changed little. When Hubble developed his original morphological system, his sample consisted of mostly nearby, luminous galaxies with only 3% "irregular" galaxies. These galaxies were not well incorporated in his sequence, but for his purposes the morphological system developed was adequate for classifying 97% of his sample.

As deeper galaxy catalogs emerged, however, more and more galaxies fell into the catch-all, irregular morphological class. Today, *Hubble Space Telescope* (*HST*) imaging reveals that a large fraction of distant galaxies have morphologies that do not fit into the elliptical-spiral Hubble sequence. The Hubble sequence also fails to be useful when classifying galaxies in clusters, with most galaxies classified as S0 or E, which fail to account for the wide range of cluster galaxy properties (e.g., Koopmann & Kinney 1998). Spectral parameters are often more useful in these cases (e.g., Dressler & Gunn 1992). Today we classify irregular galaxies not simply in a morphological system, but with regard to the physical mechanisms in operation or the salient physical conditions (e.g., starburst galaxies, interacting galaxies, gas-rich and gas-poor galaxies). A morphological classification that reflects these physical differences would be a powerful tool for studying the mechanisms driving galaxy evolution. Such studies naturally must include high- redshift galaxies. Therefore, a morphological system that encompasses all galaxies and works sensibly over a wide range in redshift is absolutely essential, but at present does not exist.

Recently, new methods of classifying galaxies have been proposed. One line of effort has been to train artificial neural networks to reproduce the Hubble scheme in an objective way (Burda & Feitzinger 1992; Naim et al. 1995; Odewahn 1995; Odewahn et al. 1996; Serra-Ricart et al. 1993; Storrie-Lombardi et al. 1992). Spiekermann's (1992) approach using fuzzy logic was along this line. The number of galaxy images in modern surveys, such as the Sloan

Digital Sky Survey, will be enormous, and such automatable methods of morphological classification are desirable. However, a Hubble classification carries with it the limitations mentioned above; a system that can classify galaxies in a straightforward and quantitative manner that is based on a sound physical and morphological basis would be preferable.

Another approach to galaxy classification has been to develop sets of quantitative measures of the bulk image structures of galaxies. These methods have the potential to either replace, modify, or improve the current Hubble scheme. The new classifications generally rely on a set of photometric and/or spectral properties that are internally correlated, and correspond also with the apparent morphology of galaxies. Morgan's (1958, 1959) use of central light concentration was the first example of such a classification. Indeed, the use of concentration indices for inferring the morphology of galaxies has continued to improve and, along with surface brightness and asymmetry, has become one of the major tools for classifying both nearby and distant galaxies (e.g., Okamura, Kodaira, & Watanabe 1984; Doi et al. 1993; Abraham et al. 1994; Bershady et al. 2000). A different method applicable for spirals has been suggested by Elmegreen & Elmegreen (1982): measures of spiral arm morphology, particularly their patchiness, can be used for classification. Related attempts to classify galaxies have included the use of principal-component analysis of photometric structures (Whitmore 1984; Watanabe et al. 1985; Han 1995). These systems revealed correlations of physical and morphological features of galaxies, but have not been generally adopted for practical use, and the basic Hubble (1926) system lives on.

A key element missing from the recent work listed above is the connection made by Morgan between image structure and stellar content (i.e., between light concentration, or central surface brightness, and spectral type). Ironically, parallel to the above efforts to quantify image structure, there has been considerable effort to develop quantitative methods of spectral classification based on broadband colors (Bershady 1995) and spectra (Connolly et al. 1995; Zaritsky et al. 1995; Folkes et al. 1996; Bromley et al. 1998; Ronen, Aragon-Salamanca, & Lahav 1999). What is needed, then, is to go full circle to where Morgan left off by tying together the spectral types with the quantitative classification–based image structure. Here, we propose that using a measure of asymmetry and color for galaxies is a powerful method toward accomplishing this goal. In an accompanying paper (Bershady et al. 2000) we explore the additional parameters of size, surface brightness, and image concentration.

1.2. *Asymmetry as a Physical Classifier*

Symmetry has always been one the most basic features and assumptions of most galaxy morphology systems, but also one of the most overlooked for more detailed study. The earliest galaxy morphology papers by Curtis (1918) and Hubble (1926) described galaxies in terms of their symmetry, in most cases a 180° symmetry. Hubble (1926) describes elliptical and spiral galaxies in their most basic terms as systems "characterized by rotational symmetry about dominating nuclei." In fact, it is striking how symmetric galaxy systems are and, as we will show, almost always have a minimum asymmetry at a 180° rotation angle.

Models of galaxies often assume that the mass distribution of a galaxy is symmetric. Galaxies are, to first order, dynamically relaxed systems. Understanding how and in what manner the distribution of galaxy light is asymmetric can help reveal dynamical processes in galaxies. For example, galaxies disturbed by interactions or mergers will tend to have large asymmetries. For quite some time there has been considerable effort to characterize the asymmetry in H I gas in spiral galaxies (e.g., Baldwin, Lynden-Bell, & Sancisi 1980; Richter & Sancisi 1994); attempts to do this in optical light are relatively recent (e.g., Rix & Zaritsky 1995; Kornreich, Haynes, & Lovelace 1998; Rudnick & Rix 1998). While H I studies benefit directly from kinematic data, optical studies offer complementary information since optical photons predominantly come from stars, which are collisionless and are believed to trace well the underlying matter distribution in the disk.

The quantitative use of asymmetry as a morphological parameter was used first by Schade et al. (1995) as a characterization of distant galaxies observed with the *HST*. Further use of symmetry for galaxies in deep *HST* images has been carried out by Abraham et al. (1996a, hereafter A96, 1996b) and van den Bergh et al. (1996). These papers, however, use asymmetry only as a crude, type characterization of distant galaxies in the framework of the Hubble sequence.

Attempts to characterize asymmetry for nearby galaxies, and its usefulness as a morphological parameter within existing frameworks, was first carried out by Conselice (1997, hereafter C97). In C97 it was shown that asymmetry increased with Hubble type, but with a large spread. Potentially more important was the strong correlation found between color and asymmetry, and a lack of a strong correlation between luminosity and asymmetry for the narrow absolute magnitude of the C97 sample.

In this paper we further investigate the relationship between asymmetry and other physical parameters, such as color and luminosity, and the usefulness of asymmetry as a morphological parameter. From these results, our expectations are that asymmetry can be incorporated as a pillar of a new classification system that better describes and correlates with physical features and parameters than the Hubble sequence.

The paper proceeds as follows. The calibration data set of local galaxies used for this study is described in the next section. In § 3, we then compare different methods for computing asymmetry and propose a new procedure for measuring asymmetry as a robust quantity. This method includes an iterative scheme for finding the center of rotation (§ 3.3), a noise correction (§ 3.4), and a well-defined radius of extraction. We demonstrate how asymmetry changes as a function of both the rotation angle used to compute it (§ 4.1), and as a function of galactic radius (§ 4.2). We also discuss the correlation between asymmetry and other physical parameters, i.e., the $B-V$ color of a galaxy (§ 4.3), the Hubble type, and the concentration of light (§ 4.4). Resolution effects are considered in § 5. In § 4.3 we also discuss the causes of asymmetry, concluding that asymmetries are produced by either star formation in spiral arms or dynamical effects related to interactions with other galaxies. We show these two causes may be distinguishable by examining a galaxy's position in a color-asymmetry diagram. These results are directly applicable to distant galaxies with resolved structure, such as those in the Hubble Deep Field (HDF).

TABLE 1

ASYMMETRIES AND PHYSICAL DATA FOR FREI ET AL. LOWELL SAMPLE

Index	NGC Number	Type	Notes	$A(R)_{180}$	$A(J)_{180}$	$A(R)_{90}$	$A(J)_{90}$	$B-V$	D(Mpc)	M_B
1.......	2683	SA(rs)b	EO	0.18 ± 0.01	0.23 ± 0.01	1.06 ± 0.02	1.01 ± 0.02	0.89	5.7	−18.96
2.......	2715	SAB(rs)c	...	0.18 ± 0.02	0.23 ± 0.02	0.81 ± 0.04	0.84 ± 0.03	0.54	20.4	−20.08
3.......	2768	SO(1/2)	LINER	0.03 ± 0.01	0.02 ± 0.01	0.62 ± 0.03	0.65 ± 0.04	0.92	23.7	−21.13
4.......	2775	Scd	...	0.05 ± 0.01	0.07 ± 0.01	0.15 ± 0.02	0.17 ± 0.03	0.87	17.0	−20.13
5.......	2976	SAc	pec	0.13 ± 0.02	0.20 ± 0.01	0.74 ± 0.03	0.82 ± 0.02	0.64	2.1	−16.13
6.......	2985	(R')SA(rs)ab	...	0.05 ± 0.01	0.05 ± 0.03	0.10 ± 0.03	0.09 ± 0.06	0.71	22.4	−20.65
7.......	3077	I0	pec	0.22 ± 0.00	0.25 ± 0.01	0.29 ± 0.02	0.29 ± 0.02	0.69	2.1	−16.13
8.......	3079	SB(s)c	EO, Sy2	0.48 ± 0.01	0.53 ± 0.01	1.20 ± 0.04	1.23 ± 0.06	0.	20.4	−21.01
9.......	3147	SA(rs)bc	Sy2	0.09 ± 0.01	0.09 ± 0.04	0.09 ± 0.05	0.03 ± 0.13	0.79	40.9	−21.73
10......	3166	SA(rs)0/a	LINER	0.06 ± 0.00	0.07 ± 0.02	0.21 ± 0.01	0.18 ± 0.02	0.92	22.0	−20.22
11......	3184	SAB(rs)cd	...	0.17 ± 0.05	0.24 ± 0.04	0.25 ± 0.09	0.37 ± 0.13	0.58	8.7	−19.34
12......	3344	(R)SAB(r)bc	...	0.22 ± 0.01	0.15 ± 0.03	0.21 ± 0.04	0.12 ± 0.11	0.58	6.1	−18.47
13......	3351	SB(r)b	...	0.06 ± 0.01	0.09 ± 0.01	0.18 ± 0.03	0.20 ± 0.03	0.80	8.1	−19.26
14......	3368	SAB(rs)ab	Sy	0.07 ± 0.01	0.09 ± 0.01	0.38 ± 0.02	0.35 ± 0.03	0.84	8.1	−19.62
15......	3377	E5-6	...	0.02 ± 0.01	0.03 ± 0.02	0.46 ± 0.04	0.45 ± 0.03	0.84	8.1	−18.55
16......	3379	E1	...	0.02 ± 0.01	0.02 ± 0.01	0.10 ± 0.02	0.09 ± 0.02	0.94	8.1	−19.39
17......	3486	SAB(r)c	Sy2	0.14 ± 0.02	0.16 ± 0.01	0.25 ± 0.06	0.26 ± 0.05	0.51	7.4	−18.61
18......	3556	SB(s)cd	EO	0.25 ± 0.01	0.26 ± 0.02	1.42 ± 0.03	0.95 ± 0.14	0.66	14.1	−20.77
19......	3596	SAB(rs)c	...	0.15 ± 0.01	0.18 ± 0.02	0.22 ± 0.02	0.23 ± 0.03	...	23.0	−20.31
20......	3623	SAB(rs)a	LINER	0.13 ± 0.01	0.15 ± 0.01	0.88 ± 0.03	0.87 ± 0.04	0.92	7.3	−19.81
21......	3631	SA(s)c	...	0.16 ± 0.02	0.23 ± 0.01	0.20 ± 0.04	0.28 ± 0.03	0.58	21.6	−20.69
22......	3672	SA(s)c	...	0.23 ± 0.01	0.27 ± 0.02	0.86 ± 0.03	0.83 ± 0.04	0.68	28.4	−21.17
23......	3675	SA(s)b	...	0.13 ± 0.03	0.25 ± 0.03	0.50 ± 0.08	0.54 ± 0.15	...	12.8	−19.84
24......	3726	SAB(r)c	...	0.18 ± 0.03	0.23 ± 0.03	0.44 ± 0.08	0.48 ± 0.07	0.48	17.0	−20.35
25......	3810	SA(rs)c	...	0.19 ± 0.01	0.22 ± 0.01	0.36 ± 0.02	0.38 ± 0.03	0.54	16.9	−20.11
26......	3877	SA(s)c	EO	0.22 ± 0.01	0.24 ± 0.01	1.22 ± 0.03	1.19 ± 0.04	0.80	17.0	−20.25
27......	3893	SAB(rs)c	...	0.19 ± 0.01	0.25 ± 0.01	0.32 ± 0.02	0.37 ± 0.02	...	17.0	−20.27
28......	3938	SA(s)c	...	0.19 ± 0.01	0.20 ± 0.01	0.18 ± 0.02	0.21 ± 0.03	0.51	17.0	−20.26
29......	3953	SB(r)bc	LINER, H II	0.13 ± 0.01	0.16 ± 0.01	0.56 ± 0.04	0.60 ± 0.04	0.76	17.0	−20.63
30......	4013	Sb	EO	0.06 ± 0.12	0.03 ± 0.10	0.05 ± 0.15	−0.02 ± 0.15	0.96	17.0	−19.55
31......	4030	SA(s)bc	...	0.11 ± 0.01	0.15 ± 0.01	0.21 ± 0.02	0.25 ± 0.02	...	25.9	−20.27
32......	4088	SAB(rs)bc	...	0.41 ± 0.01	0.43 ± 0.01	0.97 ± 0.02	0.96 ± 0.03	0.58	17.0	−20.47
33......	4123	SB(r)c	...	0.14 ± 0.03	0.18 ± 0.02	0.49 ± 0.08	0.51 ± 0.08	0.59	25.3	−20.25
34......	4125	E6	pec, LINER	0.03 ± 0.02	0.04 ± 0.01	0.30 ± 0.09	0.36 ± 0.08	0.91	24.2	−21.35
35......	4136	SAB(r)c	...	0.14 ± 0.02	0.18 ± 0.02	0.13 ± 0.05	0.15 ± 0.06	...	9.7	−18.23
36......	4144	SAB(s)cd?	EO	0.14 ± 0.03	0.17 ± 0.02	0.95 ± 0.08	0.97 ± 0.09	0.43	4.1	−16.87
37......	4157	SAB(s)b?	EO	0.29 ± 0.01	0.27 ± 0.04	1.24 ± 0.04	0.81 ± 0.13	0.80	17.0	−20.15
38......	4242	SAB(s)dm	...	0.21 ± 0.06	0.15 ± 0.07	0.35 ± 0.10	0.43 ± 0.21	0.54	7.5	−17.91
39......	4340	SB(r)0+	...	0.02 ± 0.01	0.01 ± 0.01	0.23 ± 0.04	0.23 ± 0.04	0.91	16.8	−19.17
40......	4365	E3	...	0.03 ± 0.01	0.00 ± 0.02	0.22 ± 0.03	0.10 ± 0.10	0.95	16.8	−20.52
41......	4374	E1	...	0.01 ± 0.01	0.01 ± 0.01	0.02 ± 0.08	−0.01 ± 0.12	0.94	16.8	−20.95
42......	4406	S0(3)/E3	...	0.03 ± 0.02	0.02 ± 0.02	0.21 ± 0.05	0.16 ± 0.10	0.93	16.8	−21.15
43......	4429	SA(r)0+	...	0.05 ± 0.01	0.05 ± 0.02	0.66 ± 0.02	0.57 ± 0.06	0.96	16.8	−20.08
44......	4442	SB(s)0	...	0.02 ± 0.00	0.05 ± 0.02	0.43 ± 0.01	0.42 ± 0.02	0.93	16.8	−19.84
45......	4449	IBm	...	0.26 ± 0.01	0.29 ± 0.01	0.70 ± 0.03	0.74 ± 0.03	0.41	3.0	−17.66
46......	4450	SA(s)ab	LINER	0.04 ± 0.01	0.06 ± 0.01	0.41 ± 0.04	0.36 ± 0.06	0.80	16.8	−20.36
47......	4472	E2/S0(2)	...	0.02 ± 0.01	0.01 ± 0.00	0.14 ± 0.02	0.14 ± 0.02	0.96	16.8	−21.82
48......	4477	SB(s)0	...	0.02 ± 0.01	0.01 ± 0.01	0.17 ± 0.02	0.16 ± 0.03	0.94	16.8	−19.87
49......	4486	E2	pec	0.01 ± 0.01	0.02 ± 0.01	0.07 ± 0.02	0.07 ± 0.03	0.93	16.8	−21.64
50......	4487	SAB(rs)cd	...	0.12 ± 0.03	0.13 ± 0.05	0.32 ± 0.07	0.27 ± 0.10	...	19.9	−20.19
51......	4526	SAB(s)0	...	0.06 ± 0.00	0.07 ± 0.01	0.62 ± 0.01	0.59 ± 0.02	0.95	16.8	−20.55
52......	4564	E6	...	0.02 ± 0.01	0.02 ± 0.03	0.63 ± 0.03	0.55 ± 0.05	0.90	16.8	−19.30
53......	4593	(R)SB(rs)b	Sy1	0.09 ± 0.01	0.09 ± 0.01	0.47 ± 0.04	0.45 ± 0.04	...	39.5	−21.58
54......	4594	SA(s)a	LINER EO	0.16 ± 0.01	0.18 ± 0.03	0.60 ± 0.03	0.51 ± 0.09	0.98	20.0	−22.98
55......	4621	E5	...	0.02 ± 0.01	0.01 ± 0.01	0.33 ± 0.02	0.33 ± 0.02	0.92	16.8	−20.45
56......	4636	E/S0-1	LINER	0.02 ± 0.01	0.01 ± 0.01	0.13 ± 0.04	0.11 ± 0.05	0.92	17.0	−20.68
57......	4710	SA(r)0+	EO	0.05 ± 0.01	0.05 ± 0.01	1.11 ± 0.01	1.11 ± 0.02	0.88	16.8	−19.36
58......	4731	SB(s)cd	...	0.18 ± 0.04	0.27 ± 0.03	0.95 ± 0.12	0.96 ± 0.13	0.41	25.9	−21.17
59......	4754	SB(r)0−	...	0.01 ± 0.00	0.00 ± 0.02	0.20 ± 0.01	0.17 ± 0.02	0.90	16.8	−19.74
60......	4826	(R)SA(rs)ab	Sy2	0.15 ± 0.01	0.20 ± 0.01	0.48 ± 0.04	0.53 ± 0.02	0.84	4.1	−19.15
61......	4861	SB(s)m	...	0.12 ± 0.11	0.14 ± 0.07	0.22 ± 0.12	0.16 ± 0.11	0.58	17.8	−18.87
62......	4866	SA(r)0+	EO, LINER	0.04 ± 0.02	0.04 ± 0.03	0.84 ± 0.04	0.88 ± 0.04	0.90	16.0	−19.06
63......	5005	SAB(rs)bc	Sy2	0.14 ± 0.01	0.20 ± 0.01	0.78 ± 0.03	0.80 ± 0.02	0.80	21.3	−21.27
64......	5204	SA(s)m	...	0.20 ± 0.03	0.25 ± 0.06	0.37 ± 0.06	0.38 ± 0.13	0.41	4.8	−16.79

TABLE 1—*Continued*

Index	NGC Number	Type	Notes	$A(R)_{180}$	$A(J)_{180}$	$A(R)_{90}$	$A(J)_{90}$	$B-V$	D(Mpc)	M_B
65......	5248	SAB(rs)bc	H II	0.18 ± 0.01	0.20 ± 0.02	0.56 ± 0.03	0.54 ± 0.07	0.65	22.7	−21.07
66......	5322	E3-4	LINER	0.02 ± 0.02	0.02 ± 0.01	0.29 ± 0.06	0.33 ± 0.06	0.89	31.6	−21.66
67......	5334	SB(rs)c	...	0.08 ± 0.12	0.09 ± 0.12	−0.07 ± 0.14	−0.09 ± 0.14	...	24.7	−19.66
68......	5364	SA(rs)bc	pec, H II	0.15 ± 0.03	0.15 ± 0.02	0.36 ± 0.07	0.31 ± 0.09	0.61	25.5	−21.17
69......	5371	SA(rs)bc	LINER	0.14 ± 0.01	0.14 ± 0.02	0.42 ± 0.03	0.38 ± 0.05	0.68	37.8	−21.57
70......	5377	(R)SB(s)a	...	0.03 ± 0.01	0.07 ± 0.02	0.67 ± 0.03	0.59 ± 0.06	0.89	31.0	−20.69
71......	5585	SAB(s)d	...	0.23 ± 0.02	0.16 ± 0.03	0.44 ± 0.06	0.34 ± 0.09	0.46	7.0	−17.96
72......	5669	SAB(rs)cd	...	0.18 ± 0.03	0.19 ± 0.06	0.42 ± 0.05	0.38 ± 0.09	...	24.9	−19.88
73......	5701	(R)SB(rs)0/a	...	0.04 ± 0.00	0.05 ± 0.02	0.27 ± 0.01	0.27 ± 0.02	0.84	26.1	−20.35
74......	5746	SAB(rs)b	EO	0.26 ± 0.01	0.25 ± 0.01	1.02 ± 0.02	1.03 ± 0.05	0.97	29.4	−21.73
75......	5792	SB(rs)b	...	0.31 ± 0.02	0.36 ± 0.03	0.65 ± 0.04	0.72 ± 0.07	0.78	30.6	−20.83
76......	5813	E1-2	...	0.02 ± 0.01	0.03 ± 0.02	0.20 ± 0.03	0.18 ± 0.05	0.94	28.5	−20.77
77......	5850	SB(r)b	...	0.07 ± 0.01	0.08 ± 0.03	0.29 ± 0.06	0.28 ± 0.11	0.74	28.5	−20.69
78......	5985	SAB(r)b	LINER	0.14 ± 0.01	0.11 ± 0.02	0.67 ± 0.03	0.49 ± 0.05	0.74	39.2	−21.42
79......	6015	SA(s)cd	H II	0.15 ± 0.01	0.19 ± 0.02	0.65 ± 0.03	0.63 ± 0.05	0.56	17.5	−20.05
80......	6118	SA(s)cd	...	0.13 ± 0.02	0.14 ± 0.04	0.80 ± 0.06	0.67 ± 0.10	0.64	25.4	−20.62
81......	6384	SAB(r)bc	...	0.14 ± 0.01	0.13 ± 0.02	0.40 ± 0.04	0.34 ± 0.07	0.61	26.6	−21.31
82......	6503	SA(s)cd	LINER, H II	0.15 ± 0.01	0.23 ± 0.01	1.04 ± 0.01	1.08 ± 0.03	0.68	6.1	−18.64

2. CALIBRATION DATA SET

The data used in this present study are the full set of 113 galaxies in the Frei et al. (1996) catalog (hereafter referred to as the Frei sample). In contrast, C97 was limited to face-on spiral galaxies or elliptical galaxies from the same sample; inclined systems, irregular galaxies, and active galaxies were left out.

2.1. *Photometry*

The current sample under study consists of 82 galaxies imaged in the B_J and R bands (Gullixon et al. 1995) and 31

TABLE 2

Asymmetries and Physical Data for Frei et al. Palomar Sample

Index	NGC Number	Type	Notes	$A(g)_{180}$	$A(r)_{180}$	$A(i)_{180}$	$A(r)_{90}$	$B-V$	D(Mpc)	M_B
1.......	2403	SAB(s)cd	...	0.30 ± 0.02	0.17 ± 0.03	0.10 ± 0.05	0.53 ± 0.00	0.47	4.2	−19.68
2.......	2541	SA(s)cd	...	0.16 ± 0.10	0.17 ± 0.10	0.08 ± 0.13	0.56 ± 0.02	0.46	10.6	−18.37
3.......	2903	SAB(rs)bc	H II	0.22 ± 0.01	0.16 ± 0.01	0.12 ± 0.02	0.63 ± 0.00	0.67	6.3	−19.85
4.......	3031	SA(s)ab	LINER	0.08 ± 0.01	0.06 ± 0.01	0.05 ± 0.01	0.63 ± 0.00	0.95	1.4	−18.29
5.......	3198	SB(rs)c	...	0.14 ± 0.05	0.12 ± 0.04	0.07 ± 0.06	0.75 ± 0.00	0.54	10.8	−19.62
6.......	3319	SB(rs)cd?	H II	0.13 ± 0.09	0.10 ± 0.09	0.04 ± 0.13	0.83 ± 0.01	0.41	11.5	−18.71
7.......	4178	SA(rs)dm	...	0.24 ± 0.05	0.21 ± 0.04	0.13 ± 0.07	1.00 ± 0.00	0.49	16.8	−19.77
8.......	4189	SAB(rs)cd?	EO	0.33 ± 0.03	0.32 ± 0.03	0.22 ± 0.04	0.44 ± 0.00	0.77	16.8	−18.72
9.......	4192	SAB(s)ab	H II	0.25 ± 0.03	0.20 ± 0.02	0.14 ± 0.03	0.44 ± 0.00	0.81	16.8	−21.08
10......	4216	SAB(s)b	H II, EO	0.28 ± 0.01	0.21 ± 0.01	0.15 ± 0.01	0.64 ± 0.00	0.98	16.8	−20.96
11......	4254	SA(s)c	...	0.36 ± 0.01	0.31 ± 0.01	0.22 ± 0.02	0.36 ± 0.00	0.57	16.8	−20.84
12......	4258	SAB(s)bc	Seyfert	0.23 ± 0.01	0.19 ± 0.01	0.13 ± 0.01	0.58 ± 0.00	0.69	6.8	−20.59
13......	4303	SAB(rs)bc	H II	0.30 ± 0.01	0.28 ± 0.01	0.20 ± 0.02	0.40 ± 0.00	0.53	15.2	−20.71
14......	4321	SAB(s)bc	H II	0.18 ± 0.03	0.16 ± 0.02	0.10 ± 0.04	0.35 ± 0.00	0.70	16.8	−21.13
15......	4394	(R)SB(r)b	LINER	0.06 ± 0.01	0.05 ± 0.01	0.04 ± 0.01	0.23 ± 0.00	0.85	16.8	−19.49
16......	4414	SA(rs)c?	...	0.21 ± 0.01	0.15 ± 0.01	0.10 ± 0.01	0.43 ± 0.00	0.84	9.7	−19.12
17......	4498	SAB(s)d	...	0.16 ± 0.04	0.15 ± 0.04	0.10 ± 0.06	0.75 ± 0.00	...	16.8	−18.93
18......	4501	SA(rs)b	syft	0.21 ± 0.02	0.16 ± 0.01	0.12 ± 0.02	0.52 ± 0.00	0.73	16.8	−21.23
19......	4527	SAB(s)bc	H II	0.25 ± 0.03	0.20 ± 0.02	0.17 ± 0.03	0.63 ± 0.00	0.86	13.5	−19.72
20......	4535	SAB(s)c	...	0.15 ± 0.04	0.13 ± 0.03	0.08 ± 0.06	0.39 ± 0.00	0.63	16.8	−20.60
21......	4548	SB(rs)b	LINER	0.08 ± 0.03	0.06 ± 0.03	0.05 ± 0.04	0.25 ± 0.00	0.81	16.8	−20.28
22......	4559	SAB(rs)cd	...	0.22 ± 0.03	0.20 ± 0.02	0.11 ± 0.04	0.69 ± 0.00	0.45	9.7	−20.07
23......	4569	SAB(rs)ab	LINER	0.15 ± 0.03	0.13 ± 0.02	0.09 ± 0.03	0.69 ± 0.00	0.72	16.8	−21.27
24......	4571	SA(r)d	...	0.08 ± 0.07	0.07 ± 0.06	0.03 ± 0.09	0.20 ± 0.01	0.51	16.8	−19.38
25......	4579	SAB(rs)b	LINER	0.06 ± 0.02	0.05 ± 0.01	0.04 ± 0.02	0.27 ± 0.00	0.82	16.8	−20.67
26......	4651	SA(rs)c	LINER	0.11 ± 0.03	0.10 ± 0.02	0.07 ± 0.03	0.33 ± 0.00	0.57	16.8	−20.07
27......	4654	SAB(rs)cd	...	0.20 ± 0.04	0.19 ± 0.04	0.11 ± 0.06	0.63 ± 0.00	0.60	16.8	−20.31
28......	4689	SA(rs)bc	...	0.07 ± 0.08	0.05 ± 0.06	0.02 ± 0.08	0.23 ± 0.01	0.65	16.8	−19.62
29......	4725	SAB(r)ab	pec	0.08 ± 0.05	0.07 ± 0.03	0.05 ± 0.04	0.34 ± 0.00	0.72	12.4	−20.65
30......	5033	SA(s)c	Seyfert	0.18 ± 0.05	0.15 ± 0.03	0.10 ± 0.04	0.53 ± 0.00	0.55	18.7	−21.03
31......	5055	SA(rs)bc	H II	0.19 ± 0.02	0.14 ± 0.02	0.10 ± 0.02	0.43 ± 0.00	0.72	7.2	−20.14

in the Gunn g, r, and i bands. The scale for the B_J and R images is 1".34 pixel^{-1} with a field of view of 7' × 11'; for the g, r, and i images the scale was 1".19 pixel^{-1} with a field of view of 16' × 16'. The g, r, and i images have relatively lower signal-to-noise ratio (S/N) than the B_J and R images because of substantially shorter exposures times. In addition to the usual processing (bias subtraction and flat-fielding), Frei et al. removed foreground stars. Occasionally, a star that is projected on a bright part of the nucleus was not removed and causes a false high value for the asymmetry number for those galaxies.

For consistency between the above photometric subsets, we use the $B-V$ colors listed in the Third Reference Catalogue of Bright Galaxies (de Vaucouleurs et al. 1991, hereafter RC3) for purely photometric purposes. (Structural parameters are computed from the images described above.) The adopted $B-V$ colors are observed, i.e., uncorrected for Galactic and internal extinction, and heliocentric velocity (the k-correction). These corrections are small and hence have no qualitative impact on the conclusions of this paper. We adopt the distances and B absolute magnitudes given by Tully (1988). We note, however, that these M_B include the above corrections. (A more consistent treatment is presented in Bershady et al. 2000.) The adopted values of M_B, $B-V$, and distance are listed in Tables 1 and 2.

2.2. *Sample Characteristics*

The Frei sample includes Hubble types from early ellipticals and S0s to late-type spirals, irregulars, and galaxies with peculiar features. Several of the galaxies in the sample contain features such as rings and bars. Most of the galaxies in the sample are nearby, with a large portion of the ellipticals coming from the Virgo cluster. All of the galaxies were chosen away from the galactic equator and are generally near the northern Galactic cap. However, the Frei sample consists only of bright, high surface brightness galaxies. Hence, we are not considering the large population of low surface brightness or dwarf galaxies that make up the bulk of all galaxies in the universe. It is important to realize that the Frei sample is not likely to be an accurate representation of the entire local galaxy population, but only samples a range of Hubble types for the brightest, nearby galaxies.

For illustrative purposes, in the remainder of this paper we have selected 21 galaxies that are representative examples of total sample of 113 used in this study. These 21 galaxies span T-types, inclinations, and colors.[1]

3. ASYMMETRY ALGORITHM

The asymmetry A_ϕ, where ϕ is the angle of rotation, is a quantitative parameter based on comparing a source image with its rotated counterpart. In principle, A_ϕ is straightforward and quick to measure in its simplest form. We compare several different methods, including those presented by Abraham et al. (1996a) and C97 in the context of a $\phi = 180°$ rotation to determine if they are robust morphological measures over a range of astronomical conditions. On this basis, we develop a more sophisticated approach, ultimately based on the algorithm of A96.

3.1. *Image Preparation*

Before a rotational asymmetry measurement can be made, basic digital image processing must be completed (i.e., bias subtraction, flat-fielding, fringe correction, cosmic-ray removal, and bad pixel interpolation). In addition, any objects in the galaxy's image that are not part of the galaxy, such as foreground stars or foreground and background galaxies, must be removed by blanking the contaminated portion of the images or subtracting the contaminating source. Contaminating sources tend to be at random locations with respect to the primary source, hence residuals from this decontamination process will add to the asymmetry depending on their amplitude relative to the source brightness. In the case of unresolved contaminating sources, e.g., stars, the removal is straightforward. Foreground and background galaxies are more difficult to remove or exclude both because of their more complex and extended image structure and because their identification as separate from the primary source can require further information and judgment. This complication becomes particularly important in ultradeep images such as the HDF, but we do not pursue this further here as it is not an issue for the current study.

In addition to any foreground stellar images, the mean background level for each image must be carefully subtracted. This will become clear in the next section, where we define the specific computational algorithm. A significant nonzero background level can radically alter the measured asymmetry value. After a successful background subtraction and object decontamination, however, it is then possible to perform the asymmetry measurement without further image calibration or processing.

3.2. *Methods of Computation*

The rotational asymmetry measurement procedure consists of (1) defining an image center and "extraction" region, (2) rotating the image about this center by angle ϕ, and (3) performing a comparison of the resultant rotated image with the original image within the extracted region. This comparison, however, can have several mathematical forms. In published studies (e.g., C97, A96), the comparison is made by subtracting the rotated image from the original, although in principle the product or ratio might be useful. We have found that only subtraction appears to work well, and discuss only this possible algorithm further. The details of the centering and choice of rotation angle (§ 3.3 and § 4.1, respectively) are critical, but do not depend on the mathematical form of the asymmetry algorithm.

Once the rotated image is subtracted from the original image, we then have a residual image of all asymmetric features of the galaxy. The asymmetry measurement is completed by measuring the amplitude of the pixel values in the residual image, and normalizing this amplitude by a corresponding measure in the original image. Here again, several mathematical possibilities exist.

The method used in C97 consists of summing the square of the pixels in the residual image, and normalizing this value by dividing by the sum of the square of the pixels in the original image. Since the pixel values in the residual image will be, on average, half-negative and half-positive pixel values, half the above ratio gives the asymmetry number for that galaxy as

$$A_{\rm rms}^2 = \frac{\Sigma(I_o - I_\phi)^2}{2\Sigma I_o^2} ,$$

where I_o is the intensity distribution in the original image, and I_ϕ is the intensity distribution in the image rotated by

---

[1] The remaining sample can be viewed at http://astro.Princeton.EDU/~frei/galaxy_catalog.html.

angle ϕ. The sum is over all pixels within a prescribed, matching region of the original and rotated images. We will call this procedure the “ rms ” asymmetry method.

Operationally similar, is to replace the square by the absolute value, as done by Schade et al. (1995) and A96. Instead of using a sum of squares of the original image, a sum of the absolute value is used to normalize the residuals:

$$A_{\mathrm{abs}} = \frac{\Sigma |I_o - I_\phi|}{2\Sigma |I_o|}\,.$$

Again, the sum is over all pixels within a prescribed, matching region of the original and rotated images. We will call this procedure the “ abs ” asymmetry method.

For both methods the lowest possible value for the asymmetry parameter is 0, while the highest is 1. A value of 0 corresponds to a galaxy that is completely symmetric; that is, the difference $I_o - I_\phi = 0$ at all points in the difference image formed from subtracting the rotated image from the original image. A values of 1 correspond to a galaxy that is completely asymmetric such that, on average, $|I_o - I_\phi| = I_o$. Values for most galaxies lie between these two extremes (see Tables 1, 2, 3, and 4 for $\phi = 90°$ and 180°).

Comparing the above two asymmetry computations for $\phi = 180°$ rotations, we find that the values for A_{abs} are similar to the values found for A_{rms}, as measured in the red. The A_{abs} values have slightly larger asymmetries at high A, as can be seen in Figure 1 from the positive value of $A_{\mathrm{abs}} - A_{\mathrm{rms}}$ at large A_{rms}. As a function of wavelength, the rms asymmetries show a clear trend toward higher differences in A(blue, herafter B) $-A$(red, hereafter R) at larger (red) asymmetries, as seen in Figure 2; this can be seen to a lesser extent for the abs method in Figure 3. (Here blue corresponds either to the B or g bands, and red corresponds to either R or r bands.) The average difference in $A(B) - A(R)$ for the rms method is 0.015 overall, and 0.05 at $A(\mathrm{red}) > 0.1$. The abs method yields asymmetries that are fairly constant between bands with an average $A(B) - A(R)$ of 0.005 over all asymmetry values.

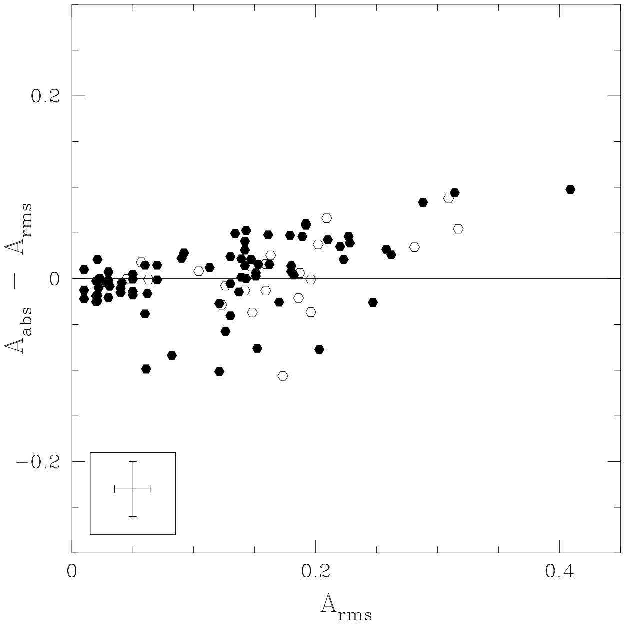

FIG. 1.—Scatter plot of the red 180° asymmetries computed by the rms method (Conselice 1997) and the abs method (Abraham et al. 1996a). The two methods produce similar asymmetry values, with a noticeable trend toward higher asymmetries for more asymmetric galaxies. The open symbols are Palomar sample galaxies (Gunn r band, Table 2); filled symbols are the Lowell sample galaxies (R band, Table 1).

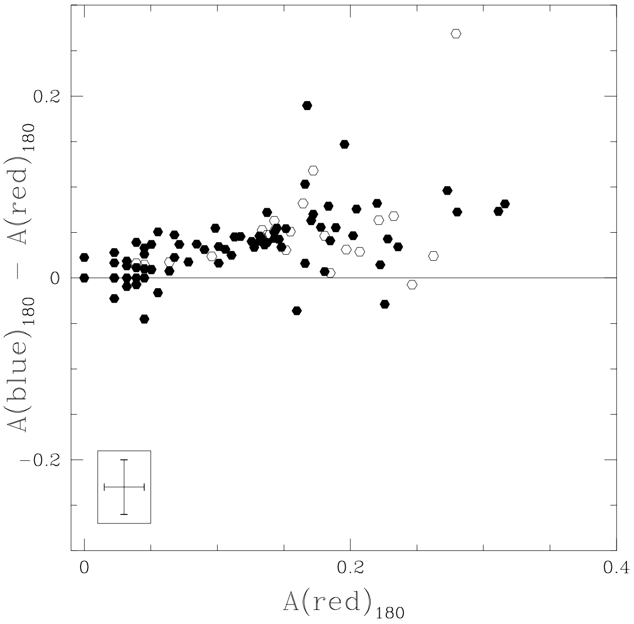

FIG. 2.—Comparison between the 180° rms asymmetry parameter computed in the R and B bands (*filled symbols*) and g and r bands (*open symbols*). The bluer band asymmetries tend to be more asymmetric than the redder band asymmetries, and this difference increases at higher asymmetries. This indicates that young blue stars (and, therefore, recent star formation) produce asymmetries. There is no difference in trend or scatter between the B vs. R and g vs. r data.

However, we find that the abs method gives a tighter correlation between asymmetry and color than the rms method, contrary to our expectations. The rms method was expected to be a better indicator of star formation since it weights higher the brighter, asymmetric features. The brightness of a star-forming region in a galaxy is a function

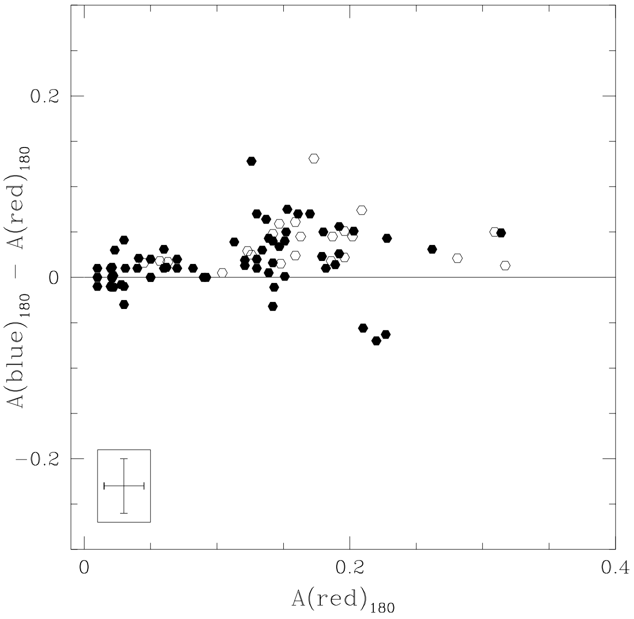

FIG. 3.—As Fig. 2, but with the asymmetries computed with the abs method. The relationship between the asymmetries does not show the prominent rise in blue asymmetries as the rms asymmetry values.

TABLE 3

ASYMMETRIES CACLULATED AT VARIOUS RADII FOR THE FREI ET AL. LOWELL SAMPLE[a]

Index	NGC Number	$A(\eta = 0.8)$	$A(\eta = 0.5)$	$A(\eta = 0.2)$	$A(g = 20\%)$	$A(g = 50\%)$	$A(g = 80\%)$	$A_\eta^{\rm b}$	$A_g^{\rm c}$
1	NGC 2683	0.120	0.155	0.183	0.144	0.161	0.183	0.172	0.175
2	NGC 2715	0.486	0.146	0.175	0.098	0.137	0.149	0.206	0.192
3	NGC 2768	0.021	0.015	0.026	0.015	0.014	0.025	0.036	0.029
4	NGC 2775	0.031	0.019	0.052	0.018	0.051	0.051	0.062	0.057
5	NGC 2976	0.119	0.135	0.127	0.116	0.127	0.134	0.119	0.119
6	NGC 2985	0.031	0.039	0.046	0.039	0.045	0.045	0.046	0.046
7	NGC 3077	0.044	0.138	0.219	0.139	0.209	0.213	0.222	0.218
8	NGC 3079	0.108	0.324	0.476	0.231	0.394	0.472	0.483	0.478
9	NGC 3147	0.036	0.038	0.090	0.051	0.079	0.090	0.098	0.094
10......	NGC 3166	0.033	0.040	0.056	0.040	0.060	0.055	0.049	0.052
11......	NGC 3184	0.043	0.151	0.165	0.089	0.146	0.160	0.165	0.165
12......	NGC 3344	0.045	0.032	0.218	0.196	0.176	0.207	0.219	0.219
13......	NGC 3351	0.137	0.102	0.059	0.094	0.056	0.057	0.061	0.059
14......	NGC 3368	0.057	0.070	0.070	0.076	0.059	0.068	0.069	0.069
15......	NGC 3377	0.044	0.038	0.021	0.034	0.023	0.021	0.027	0.024
16......	NGC 3379	0.028	0.020	0.020	0.020	0.016	0.019	0.028	0.024
17......	NGC 3486	0.047	0.084	0.139	0.051	0.099	0.130	0.138	0.139
18......	NGC 3556	0.107	0.252	0.250	0.246	0.250	0.250	0.250	0.250
19......	NGC 3596	0.035	0.152	0.154	0.106	0.126	0.158	0.148	0.146
20......	NGC 3623	0.044	0.107	0.127	0.077	0.123	0.124	0.123	0.126
21......	NGC 3631	0.030	0.052	0.162	0.064	0.120	0.168	0.147	0.145
22......	NGC 3672	0.089	0.196	0.227	0.109	0.196	0.222	0.219	0.224
23......	NGC 3675	0.071	0.238	0.133	0.231	0.140	0.133	0.133	0.133
24......	NGC 3726	0.027	0.036	0.176	0.088	0.134	0.161	0.185	0.183
25......	NGC 3810	0.043	0.107	0.194	0.077	0.155	0.181	0.192	0.194
26......	NGC 3877	0.097	0.190	0.224	0.219	0.178	0.200	0.224	0.221
27......	NGC 3893	0.027	0.100	0.194	0.075	0.105	0.193	0.183	0.186
28......	NGC 3938	0.011	0.127	0.189	0.043	0.098	0.165	0.195	0.195
29......	NGC 3953	0.030	0.035	0.127	0.049	0.078	0.114	0.122	0.124
30......	NGC 4013	0.079	0.101	0.064	0.055	0.064	0.064	0.064	0.064
31......	NGC 4030	0.028	0.097	0.108	0.067	0.097	0.107	0.103	0.105
32......	NGC 4088	0.111	0.285	0.408	0.218	0.252	0.369	0.386	0.391
33......	NGC 4123	0.080	0.066	0.135	0.061	0.109	0.134	0.140	0.140
34......	NGC 4125	0.018	0.017	0.026	0.017	0.015	0.018	0.051	0.026
35......	NGC 4136	0.029	0.121	0.140	0.049	0.115	0.137	0.136	0.137
36......	NGC 4144	0.034	0.096	0.138	0.058	0.092	0.126	0.154	0.147
37......	NGC 4157	0.122	0.260	0.287	0.247	0.273	0.283	0.312	0.304
38......	NGC 4242	0.043	0.100	0.209	0.070	0.104	0.209	0.209	0.209
39......	NGC 4340	0.029	0.030	0.022	0.029	0.019	0.021	0.027	0.025
40......	NGC 4365	0.022	0.015	0.025	0.015	0.020	0.022	0.033	0.026
41......	NGC 4374	0.021	0.020	0.011	0.016	0.012	0.012	0.014	0.013
42......	NGC 4406	0.021	0.018	0.031	0.015	0.021	0.029	0.031	0.031
43......	NGC 4429	0.061	0.094	0.053	0.094	0.068	0.052	0.057	0.055
44......	NGC 4442	0.023	0.022	0.016	0.022	0.018	0.017	0.019	0.018
45......	NGC 4449	0.085	0.219	0.263	0.149	0.225	0.264	0.258	0.261
46......	NGC 4450	0.027	0.037	0.040	0.037	0.039	0.040	0.053	0.050
47......	NGC 4472	0.015	0.010	0.017	0.010	0.010	0.014	0.026	0.019
48......	NGC 4477	0.030	0.024	0.021	0.024	0.016	0.020	0.028	0.022
49......	NGC 4486	0.010	0.018	0.009	0.019	0.011	0.010	0.011	0.009
50......	NGC 4487	0.048	0.094	0.123	0.062	0.079	0.113	0.115	0.113
51......	NGC 4526	0.070	0.092	0.058	0.092	0.078	0.059	0.053	0.056
52......	NGC 4564	0.036	0.032	0.016	0.034	0.022	0.016	0.014	0.014
53......	NGC 4593	0.054	0.046	0.085	0.037	0.034	0.071	0.089	0.088
54......	NGC 4594	0.032	0.065	0.164	0.085	0.205	0.179	0.159	0.163
55......	NGC 4621	0.039	0.034	0.020	0.032	0.019	0.020	0.020	0.019
56......	NGC 4636	0.016	0.013	0.019	0.012	0.012	0.015	0.021	0.020
57......	NGC 4710	0.083	0.055	0.048	0.065	0.052	0.048	0.048	0.048
58......	NGC 4731	0.098	0.137	0.183	0.129	0.149	0.191	0.176	0.180
59......	NGC 4754	0.027	0.023	0.014	0.025	0.017	0.014	0.013	0.014
60......	NGC 4826	0.077	0.297	0.148	0.369	0.210	0.161	0.139	0.144
61......	NGC 4861	0.105	0.092	0.118	0.096	0.121	0.142	0.118	0.118
62......	NGC 4866	0.022	0.024	0.039	0.023	0.028	0.034	0.043	0.039
63......	NGC 5005	0.122	0.168	0.136	0.173	0.171	0.143	0.127	0.133
64......	NGC 5204	0.117	0.153	0.197	0.111	0.156	0.166	0.370	0.318
65......	NGC 5248	0.060	0.065	0.176	0.103	0.140	0.179	0.176	0.177

TABLE 3—*Continued*

Index	NGC Number	$A(\eta = 0.8)$	$A(\eta = 0.5)$	$A(\eta = 0.2)$	$A(g = 20\%)$	$A(g = 50\%)$	$A(g = 80\%)$	A_η[b]	A_g[c]
66……	NGC 5322	0.043	0.028	0.017	0.025	0.020	0.017	0.020	0.017
67……	NGC 5334	0.010	0.064	0.084	0.055	0.066	0.081	0.084	0.084
68……	NGC 5364	0.011	0.121	0.152	0.077	0.116	0.138	0.147	0.147
69……	NGC 5371	0.046	0.035	0.143	0.056	0.112	0.137	0.156	0.152
70……	NGC 5377	0.055	0.056	0.034	0.047	0.029	0.032	0.040	0.034
71……	NGC 5585	0.029	0.129	0.232	0.069	0.115	0.162	0.373	0.294
72……	NGC 5669	0.019	0.165	0.182	0.052	0.093	0.162	0.193	0.196
73……	NGC 5701	0.038	0.024	0.036	0.026	0.016	0.037	0.042	0.041
74……	NGC 5746	0.093	0.312	0.259	0.294	0.311	0.258	0.270	0.258
75……	NGC 5792	0.039	0.220	0.314	0.185	0.250	0.316	0.279	0.281
76……	NGC 5813	0.034	0.026	0.023	0.022	0.017	0.021	0.030	0.026
77……	NGC 5850	0.022	0.028	0.068	0.028	0.029	0.052	0.083	0.074
78……	NGC 5985	0.018	0.097	0.137	0.054	0.086	0.117	0.197	0.181
79……	NGC 6015	0.043	0.114	0.151	0.056	0.108	0.133	0.148	0.149
80……	NGC 6118	0.009	0.099	0.129	0.058	0.096	0.131	0.118	0.121
81……	NGC 6384	0.031	0.027	0.136	0.037	0.081	0.113	0.147	0.141
82……	NGC 6503	0.142	0.156	0.153	0.141	0.157	0.152	0.175	0.168

[a] All asymmetries are computed in the *R* band.

[b] A_η is defined as $1.5r[\eta(0.2)]$.

[c] A_g is defined as $3.0r[g(0.5)]$, where $r[g(0.5)]$ is the half-light radius.

TABLE 4

Asymmetries Caclulated at Various Radii for the Frei et al. Palomar Sample[a]

Index	NGC Number	$A(\eta = 0.8)$	$A(\eta = 0.5)$	$A(\eta = 0.2)$	$A(g = 20\%)$	$A(g = 50\%)$	$A(g = 80\%)$	A_η[b]	A_g[c]
1…….	NGC 2403	0.122	0.169	0.173	0.120	0.164	0.180	0.157	0.166
2…….	NGC 2541	0.026	0.150	0.171	0.059	0.145	0.176	0.157	0.160
3…….	NGC 2903	0.097	0.171	0.159	0.158	0.161	0.161	0.145	0.146
4…….	NGC 3031	0.003	0.023	0.057	0.026	0.053	0.055	0.064	0.059
5…….	NGC 3198	0.076	0.118	0.122	0.104	0.122	0.122	0.110	0.114
6…….	NGC 3319	0.073	0.102	0.100	0.111	0.080	0.104	0.073	0.081
7…….	NGC 4178	0.059	0.143	0.212	0.110	0.133	0.192	0.181	0.203
8…….	NGC 4189	0.051	0.226	0.317	0.075	0.158	0.296	0.287	0.287
9…….	NGC 4192	0.083	0.155	0.202	0.150	0.191	0.207	0.180	0.192
10……	NGC 4216	0.009	0.078	0.209	0.139	0.250	0.218	0.187	0.213
11……	NGC 4254	0.040	0.184	0.309	0.121	0.189	0.258	0.316	0.326
12……	NGC 4258	0.055	0.189	0.187	0.208	0.182	0.191	0.178	0.183
13……	NGC 4303	0.030	0.037	0.281	0.046	0.201	0.280	0.259	0.266
14……	NGC 4321	0.057	0.114	0.159	0.080	0.139	0.160	0.151	0.151
15……	NGC 4394	0.047	0.031	0.045	0.024	0.025	0.041	0.043	0.043
16……	NGC 4414	0.028	0.149	0.147	0.142	0.159	0.150	0.141	0.143
17……	NGC 4498	0.019	0.156	0.148	0.106	0.156	0.151	0.138	0.141
18……	NGC 4501	0.018	0.153	0.163	0.158	0.155	0.163	0.152	0.154
19……	NGC 4527	0.390	0.325	0.196	0.307	0.220	0.182	0.155	0.161
20……	NGC 4535	0.065	0.060	0.126	0.068	0.100	0.122	0.112	0.117
21……	NGC 4548	0.034	0.027	0.063	0.023	0.043	0.063	0.057	0.057
22……	NGC 4559	0.081	0.146	0.196	0.126	0.139	0.172	0.187	0.194
23……	NGC 4569	0.031	0.084	0.126	0.137	0.143	0.132	0.114	0.116
24……	NGC 4571	0.014	0.049	0.072	0.028	0.048	0.061	0.076	0.076
25……	NGC 4579	0.023	0.033	0.047	0.030	0.052	0.048	0.043	0.044
26……	NGC 4651	0.035	0.099	0.104	0.078	0.105	0.099	0.094	0.095
27……	NGC 4654	0.032	0.151	0.186	0.093	0.139	0.183	0.173	0.172
28……	NGC 4689	0.024	0.061	0.054	0.069	0.061	0.053	0.053	0.054
29……	NGC 4725	0.011	0.021	0.074	0.027	0.035	0.077	0.065	0.066
30……	NGC 5033	0.046	0.097	0.145	0.142	0.133	0.141	0.131	0.134
31……	NGC 5055	0.099	0.160	0.142	0.140	0.161	0.146	0.131	0.136

[a] All asymmetries are computed in the *r* band.

[b] A_η is defined as $1.5r[\eta(0.2)]$.

[c] A_g is defined as $3.0r[g(0.5)]$, where $r[g(0.5)]$ is the half-light radius.

of the density, squared, hence the rms method should better trace higher contribution from denser regions of star formation. While either method can be used to get physical information, the better correlation of abs asymmetries with color lead us to use the abs method for the remainder of the paper.

3.3. *Centering Corrections*

One of the most crucial aspects of the rotational asymmetry computation is the choice of a center of rotation. Centers that differ by only a small amount (relative to a galaxy's characteristic size) typically produce substantially different asymmetry values. For example, a change in the center of rotation by just 1 pixel for the Frei et al. sample (roughly 1% of a half-light radius) can change the value of the asymmetry by as much as 50%. However, this becomes less of a problem when the scale of the galaxy becomes smaller, such that as the sampling decreases so does the need for precise centering.

To overcome this centering problem, we define the center of rotation to be the position that yields a minimum value for the $\phi = 180^\circ$ asymmetry. To find such a center in practice, an initial guess is made for a galaxy's rotational center. This first step can be automated by choosing the mean, or mode of the light distribution as a reasonable initial guess; our tests indicate that the initial guess does not alter the final asymmetry. In most cases, there is a clear central pixel that is approximately in the center of the galaxy, for example, the brightest pixel in the galaxy. For irregular and edge-on galaxies, however, there is not a clear-cut brightest point, or even a well-defined center, and it is for these galaxies that this method of minimum center is most effective.

Operationally, after the asymmetry is computed at that initial position, the asymmetry is computed again for centers at the surrounding eight points in a 3×3 grid. The distance from the central point to the eight surrounding points can be set at any value. In this work, we use a distance of 0.1 pixels, corresponding to roughly 0.1% of the half-light radius. We use the task ROTATE in IRAF to perform the asymmetry measurements via bilinear interpolation. If the asymmetry parameter at the center is lower than the asymmetry value at any of the eight surrounding points, then the asymmetry parameter is taken to be the value at the center. The algorithm effectively creates a synthetic grid of asymmetry values arranged by x, y center positions. If the center pixel does not give the asymmetry minimum, as is usually the case, then the procedure repeats with the new center at the pixel value where the minimum was located. This process continues until a minimum is found for the asymmetry. Once this location is found, we define this to be the "asymmetry centroid" and use that computed asymmetry for the asymmetry parameter of the galaxy.

One possible problem with this method of finding the minimum asymmetry is the existence of local asymmetry minima. We have tested this by computing the asymmetry parameter over a wide range of centers for a set of 21 representative galaxies from the Frei sample. The second columns of Figures 4–7 are pictorial representations of the asymmetries values at all pixel locations about the inner $3'' \times 3''$ of these 21 galaxies. It can be seen in these images that no significant local minima exist throughout the image. While the detailed shape of these asymmetry planes differ from galaxy to galaxy (and indeed, contain considerable information about the light distribution) a well-defined minimum exists in each case. In the presence of sufficient noise, this condition will break down. We characterize this behavior via simulations in the following section.

3.4. *Noise Corrections*

The rotational asymmetry as defined here is, by its very nature, a pixel-by-pixel difference algorithm and, therefore, can be substantially affected by noise. Clearly this effect must be accounted for if asymmetry is to be a robust classifier. An example of the effects of noise on the asymmetry value of a galaxy is illustrated in Figure 8. The effects of both correlated and uncorrelated noise are relevant. Here, however, we develop a correction for uncorrelated noise and defer handling of correlated noise to a later study on the HDF.

The effects of uncorrelated noise in practice are easy to correct by simultaneously performing the asymmetry measurement on both the source and a neighboring, blank area of the image (see A96). The method for computing the asymmetry of the blank area is the same as before with one exception: there is no normalization by the sum of the original pixels, since in the case of the sky-subtracted background, the sum is zero on average. This procedure is then repeated in a centering grid until a minimum of the noise is found, precisely the same way the minimum asymmetry of the object is found. This blank asymmetry value is then subtracted from the value measured for the object, thereby correcting statistically for the effects of uncorrelated noise present in the object image. The final formula used to compute the asymmetry can be written as

$$A_{\rm abs} = \min\left(\frac{\Sigma |I_o - I_\phi|}{\Sigma |I_o|}\right) - \min\left(\frac{\Sigma |B_o - B_\phi|}{\Sigma |I_o|}\right),$$

where I represents the image pixels, and B represents the blank region (background) pixels. Note that the possible range of asymmetry values now spans from 0 to 2. However, due to the application of the minimization condition, the values are rarely ever greater than 1, and this primarily occurs when $\phi = 90^\circ$.

When defining a blank region it is necessary to either use an extraction region the same size as the one used on the galaxy or, more practically, scale the sum of the blank region by the relative size of the object to blank region areas. The extraction region used to define the background should be big enough to be representative, but should be small and distant enough from the galaxy so as to not include any diffuse light—and, hence, gradients—from the sources. Figure 8 shows the differences between the computed asymmetry of a galaxy with added noise and the original asymmetry as a function of S/N. It can be seen from this plot that the asymmetry differences become very large at lower S/N.

To test how successful our algorithm of removing noise is at effectively reproducing the correct value for the asymmetry parameter, we artificially degraded the Frei et al. galaxy images by adding simulated, random noise. The noise-corrected asymmetry values measured in these images allowed us to assess the systematic behavior with S/N. We compute the S/N as a ratio of the signal from the galaxy within the half-light radius to the noise contribution from the sky, source, and detector read noise within the same aperture. Results of these S/N tests are shown in Figure 9.

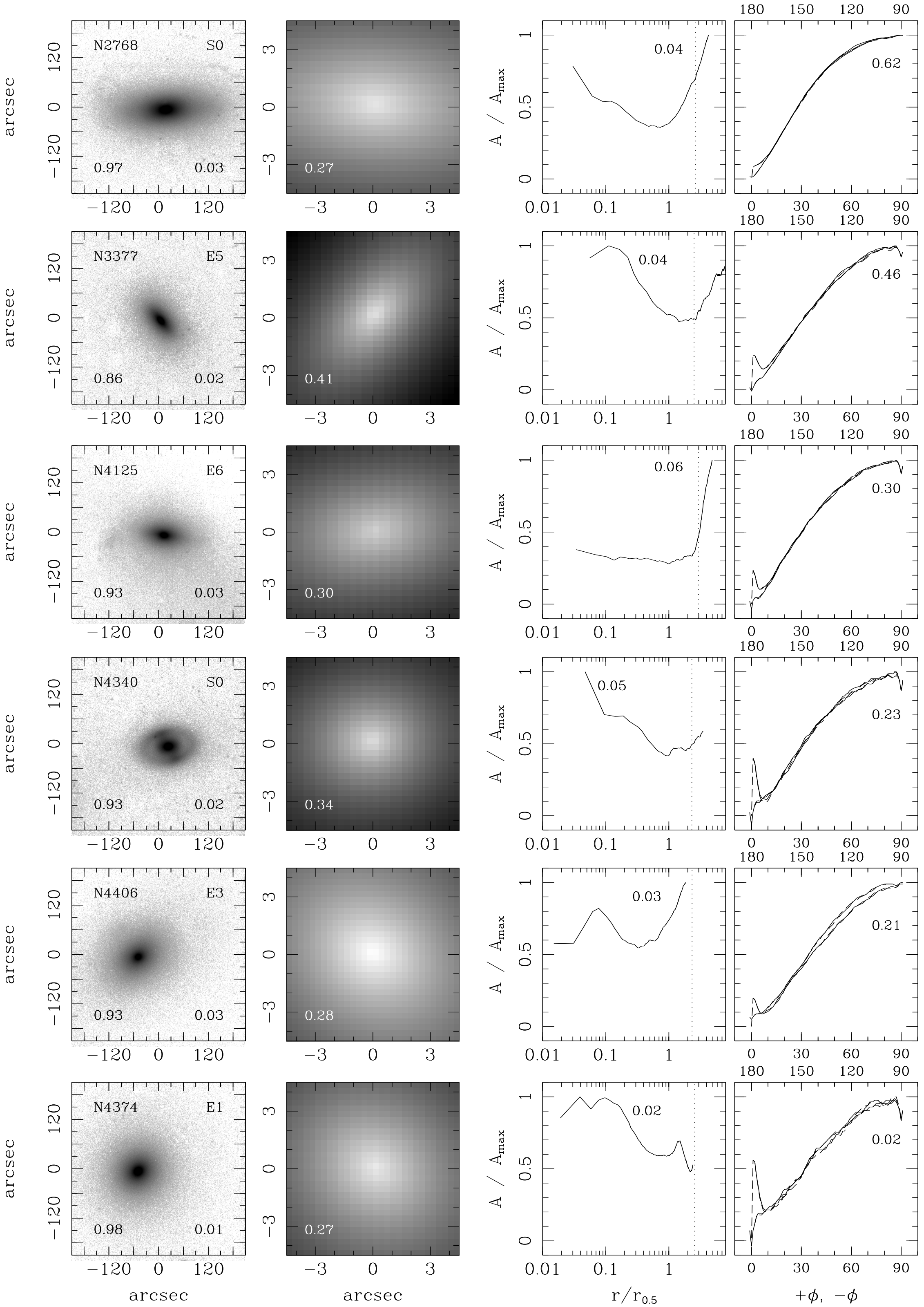

FIG. 4.—Six representative early-type galaxies from the Frei et al. (1996) sample. From left to right: (1) the B_J- or g-band image. The NGC number, Hubble type, $A_{180}(R)$, and $B-V$ color are listed in clockwise order starting at the top left corner of each image. (2) Asymmetry, $A_{180}(R)$, as a function of center position, $A(x, y)$. The gray-scale stretch is from 0.02 (*white*) to 0.44 (*black*) in every panel. The maximum asymmetry value is printed in the lower-left corner of each panel. (3) $A_{180}(R)$ / $A_{\rm max}$, the asymmetry as a function of radius (more precisely, the square extraction box half-width) normalized by the half-light radius, for rotation angle $\phi = 180$, normalized by the maximum value labeled in each panel. The radius where $\eta = 0.2$ is marked with a dotted vertical line. (4) $A_\phi(R)$ / $A_{\rm max}$, the asymmetry as a function of rotation angle ($-180 < \phi < 180$) within a radius corresponding to $\eta = 0.2$ (see text), normalized by the maximum value. $A_\phi(R)$ is folded every 90° to show the expected inherent symmetry in an axisymmetric system. Solid lines are for $0 < \phi < 180$ and dashed lines are for $-180 < \phi < 0$. The value of $A_{90}(R)$ is labeled.

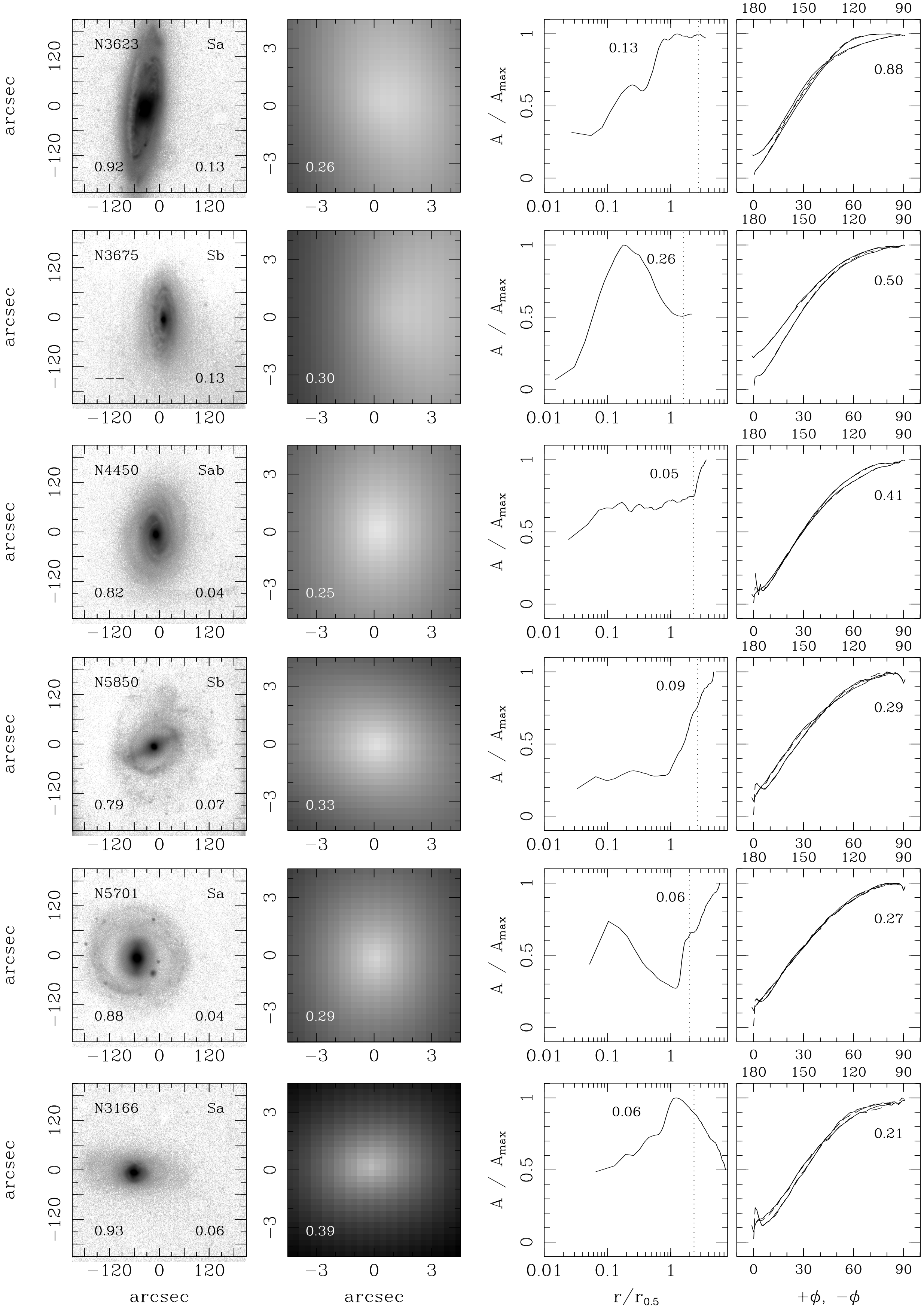

FIG. 5.—The same as Fig. 4, except for six representative intermediate-type galaxies

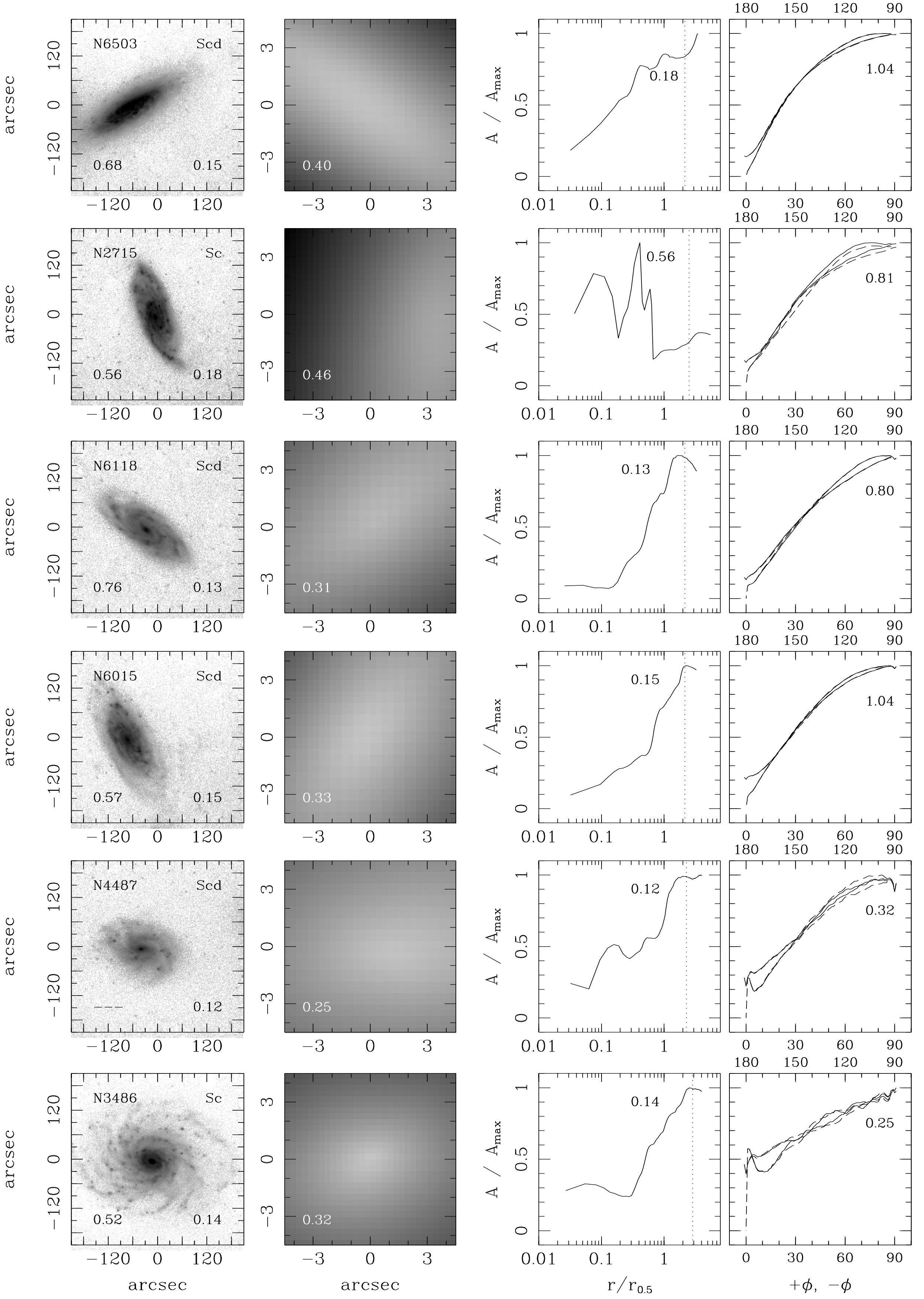

FIG. 6.—The same as Fig. 4, except for six representative late-type galaxies

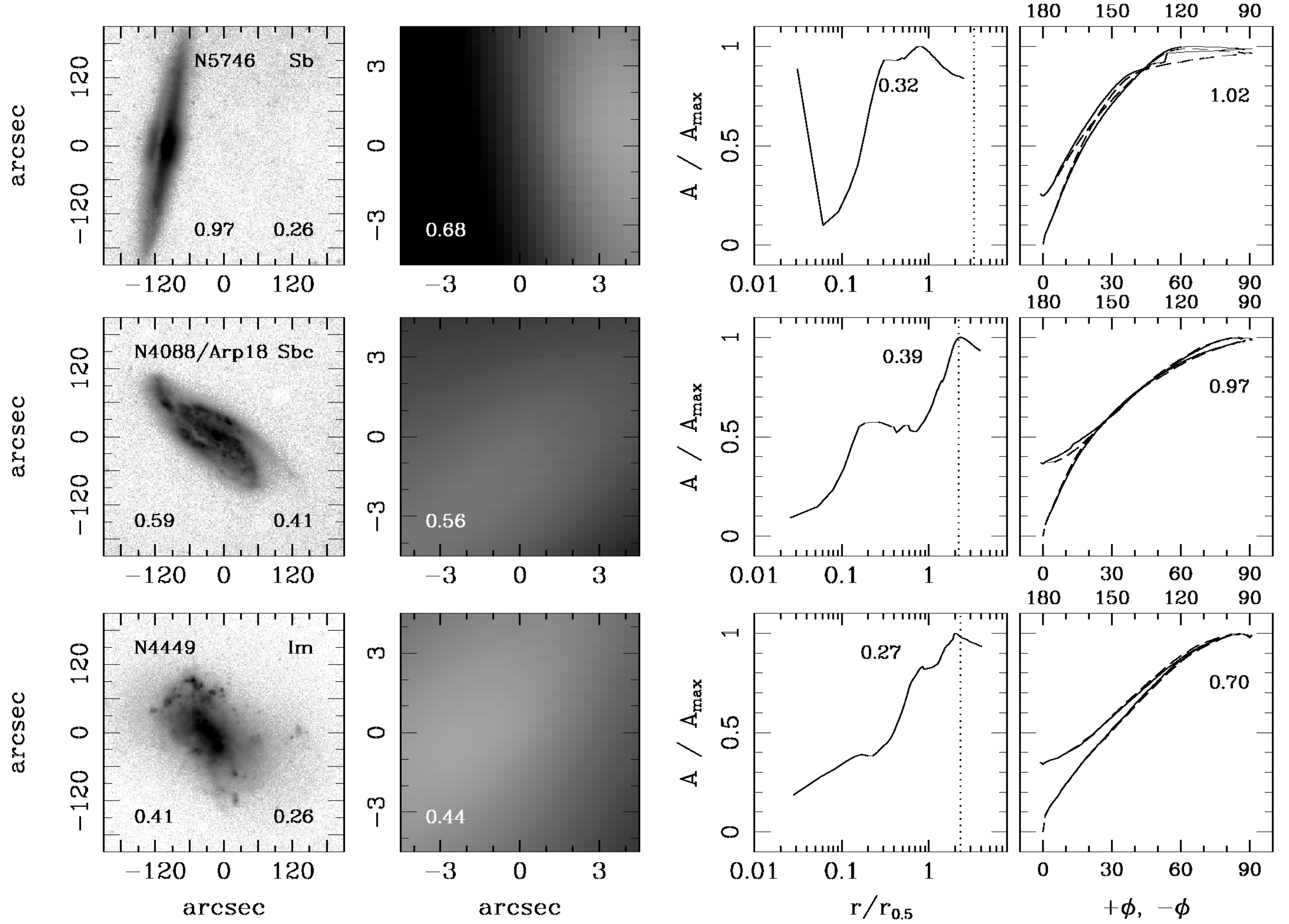

FIG. 7.—The same as Fig. 4, except for an irregular, disturbed, and edge-on galaxy

We use 35 galaxies from our sample which span all Hubble types and inclinations to perform these simulations. We find that for all of these various galaxies, the value of the asymmetry parameter found at lower S/N is, on average, still near the values found in the original images.

At signal-to-noise below ∼100, the noise begins to heavily dominate the asymmetry. In this regime, the rotation center yielding the minimum asymmetry (described in § 3.3) is determined largely by the noise field. This is compensated in the noise correction since we find the minimum again for the blank field where the background correction is calculated. If we did not recenter on the blank region when finding the background-level asymmetry, this correction would get relatively larger than the galaxy's asymmetry at successively lower S/N values. As a consequence, the corrected asymmetry would systematically become negative at low S/N values. In our current scheme, we avoid this pitfall. Even for $S/N < 100$, our simulations show that measured asymmetries have error bars that still overlap with the actual value, although the errors are very large. Errors for images with $S/N > 500$ are typically around 0.02 (rms), while with S/N between 100 and 300, errors are around 0.05 (rms). At $S/N < 100$, the error on the asymmetry becomes very high, i.e., exceeding 0.60 (rms) for $S/N < 50$. From Figure 9, however, we conclude that for all galaxies with $S/N > 100$ asymmetries can be computed reliably, which we define to be when the rms errors are less than 0.05.

A feature of our asymmetry algorithm, which comes naturally from the noise corrections, is an ability to estimate an error on the computed, corrected asymmetries. We have tested this via Monte Carlo methods and find that these estimates are accurate.[2]

4. RESULTS

The following presentation is based on the results in Tables 1 and 2, which list the asymmetry values and their estimated errors for the 113 galaxies in the Lowell and Palomar sample for $\phi = 180°$ and 90°, computed within the radius, $r(\eta = 0.2)$, and calculated as described in the previous section with centering and noise corrections. The extraction aperture based on the η-function is described in § 4.2.

4.1. *Asymmetry as a Function of ϕ*

Rotational asymmetry, as we have defined it, has heretofore been explored only in the context of 180° rotation. However, rotation by other angles can potentially yield more physical and morphological information. In particular, the azimuthal variations of galaxy light profiles can be probed, akin to the seminal work of Schweizer (1976a,

---

[2] The programs used in this paper to compute the various asymmetries can be obtained by emailing one of the authors.

1976b). While it is not our intent to pursue such a detailed study here, we do show that other angles of rotation can provide diagnostics that allow us to improve upon the utility of the 180° asymmetry correlation with color.

4.1.1. *180° Rotation: Flocculent and Dynamical Asymmetries*

The rotation of a galaxy by 180° should yield the minimum rotational asymmetry since most galaxies appear to have a strong azimuthal axisymmetry. As such, A_{180} is expected to be sensitive to either large-scale departures from axisymmetry (e.g., dynamical disturbances or asymmetric modes) or small-scale departures from axisymmetry in the form of star-forming regions. For normal galaxies, it is the latter that is of particular interest.

Both abs and rms asymmetry methods clearly show that the B_J band almost always has a higher asymmetry value than the R band (Figs. 2 and 3). This is consistent with the shorter wavelength B_J band more sensitively sampling the light from the younger stars that are distributed nonuniformly throughout the galaxy. As seen in C97, the difference between $A(B)$ and $A(R)$ increases at higher values of the asymmetry. Bershady et al. (2000) also show that the difference between $A(B)$ and $A(R)$ increases for galaxies with bluer colors. These trends are a further indication that recent star formation is the cause of asymmetries and that, for the most part, contributions to the asymmetry of normal galaxies come from blue star-forming regions in the arms of spirals or irregular galaxies. We refer to this as "flocculent" asymmetry. The vast majority of the sample have flocculent asymmetries and follow the color-asymmetry sequence as seen in Figure 10.

However, asymmetries can also be caused by dynamical events, such as the interaction or merging of two galaxies. We call the asymmetry from these interactions "dynamical" asymmetry. A dynamical event can warp and extend a galaxy, deviating its structure from the symmetric ground state. Dynamical asymmetries add to the flocculent asymmetry such that dynamically distorted galaxies have asymmetries that are always higher than asymmetries caused solely from star formation processes. The three galaxies in the Frei sample that are in the process of a galaxy interaction/merger or that are otherwise peculiar are labeled in Figure 10; they are too asymmetric for their colors. We will explore this issue, its relation to other physical features of galaxies, and how to effectively use it for morphological classification in later sections.

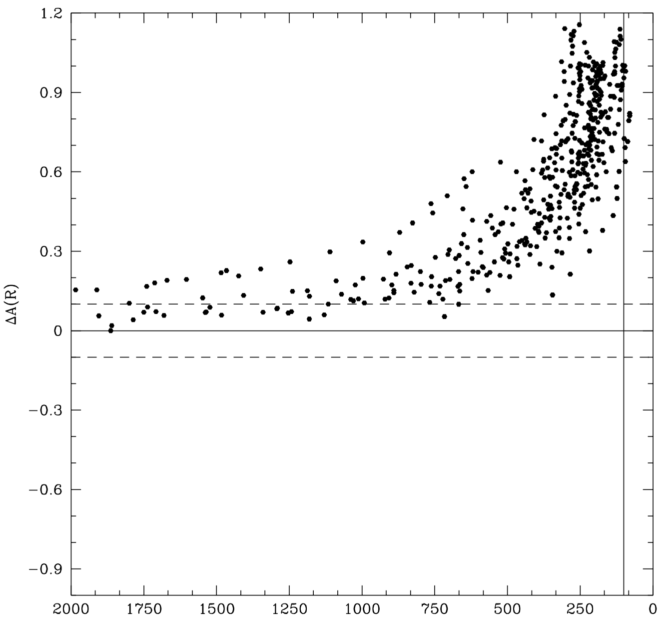

FIG. 8.—Representation of how asymmetry increases at lower values of S/N without noise corrections. Represented here are 35 galaxies from our sample which includes all inclinations and Hubble types from the entire sample. The vertical axis $\Delta A(R)$ is the difference between the computed asymmetry at a given S/N (x-axis) and the original asymmetry value. The S/N is computed within the $\eta = 0.2$ radius. The dashed lines at $\Delta A(R) = \pm 0.1$ and the vertical line at S/N of 100 are for reference. This figure shows that without correcting for the S/N, the asymmetry of a galaxy becomes large even at moderately large S/N values.

4.1.2. *90° Rotation: Ellipticity*

The asymmetry in a 90° rotation (A_{90}) is almost always larger than a 180° rotational asymmetry, as seen in Figure 11. The median ratio A_{90}/A_{180} for the Frei et al. sample is roughly 4, but has a wide range at low A_{180}. There also is a substantial range in A_{90} for galaxies spanning all values of 180° asymmetry. We interpret these observations simply to mean that galaxies have a strong 180° symmetry yet a variety of projected shapes, which leads to a wide range of 90° rotational asymmetry.

Indeed, A_{90} can be used to estimate the ellipticity of the light profile. For most normal galaxies A_{90} correlates strongly with galaxy axis ratio, b/a, as seen in Figure 13. This can also be verified by visual inspection of Figures 4–7, which are sorted (for each type) by A_{90}. There is, however, a small contribution of flocculence to A_{90}. This can be seen instead by plotting the axis ratio against the difference of A_{90} and A_{180} (Fig. 13, *bottom*). A tighter correlation can be seen between A_{90} and the axis ratio in the bottom panel after A_{90} has been corrected for the flocculent component measured by A_{180}. To first order A_{180} and A_{90} should have comparable amplitude due to flocculence alone. While we

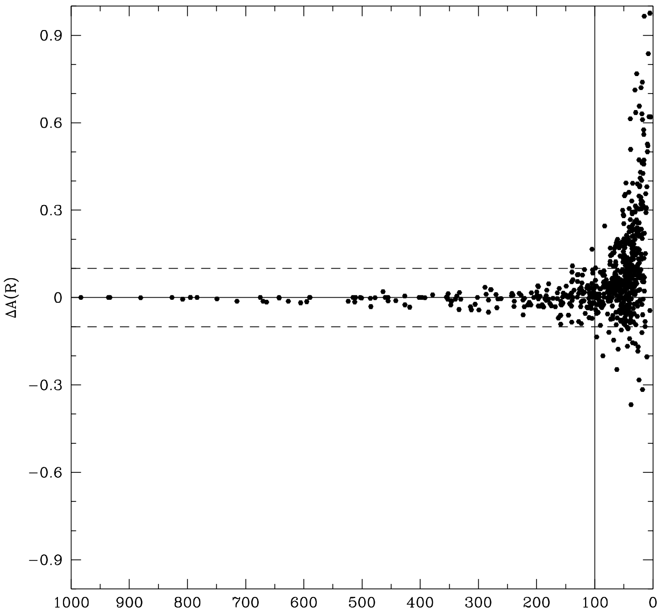

FIG. 9.—Plot of the asymmetry within the $\eta = 0.2$ radii as a function of the S/N as in Fig. 8, except here noise corrected. Reliable values, i.e. within 0.05 of the original value, of the asymmetry can be computed with the algorithm presented in this paper down to a S/N of about 100. Dashed lines at $\Delta A(R) = \pm 0.1$ and the vertical line at S/N of 100 are for reference.

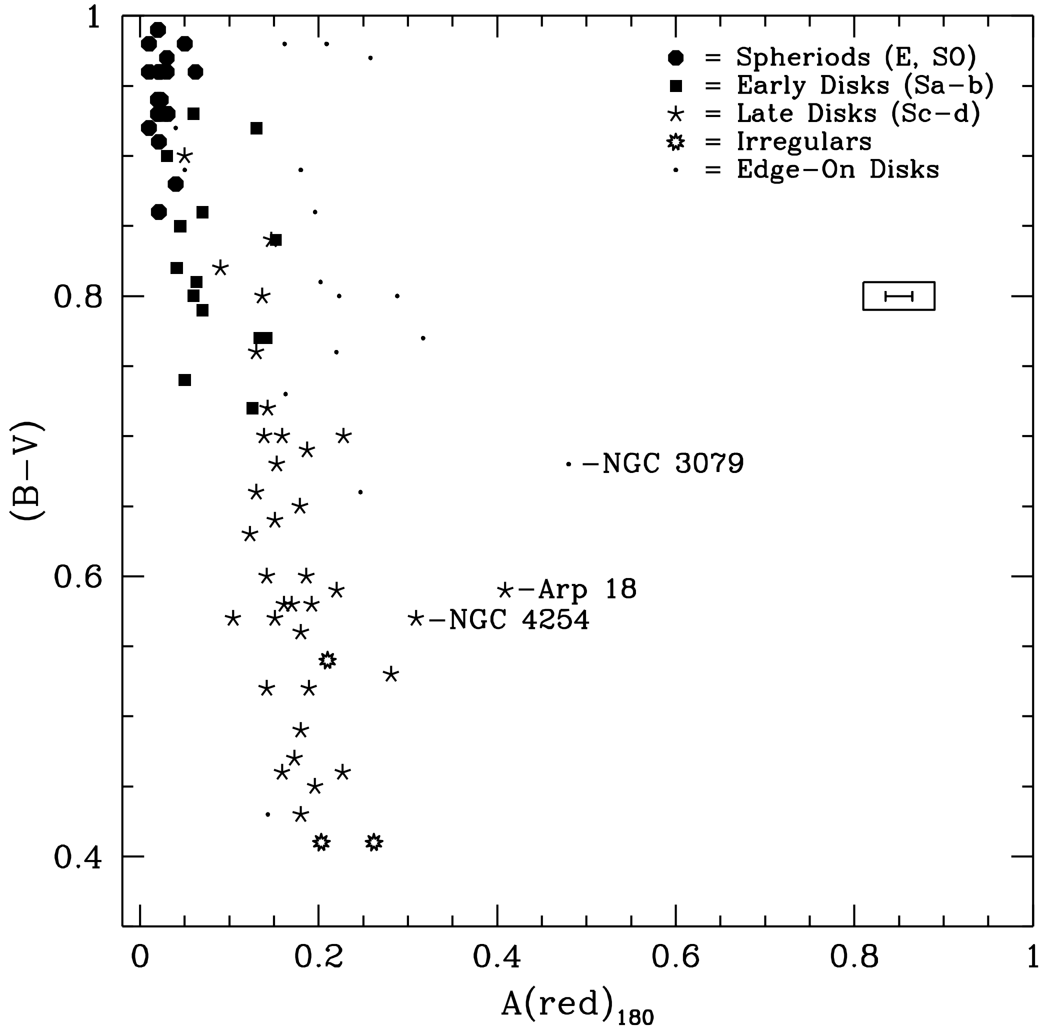

FIG. 10.—Color-asymmetry diagram. This physical-morphological diagram (as defined in text) can be used to determine the population of galaxies in a large sample. Labeled galaxies are undergoing interactions or are otherwise peculiar. Three features stand out in this diagram: (1) Early-type disks/spheriods are well separated from the late-type disks. (2) Interacting galaxies deviate from the color-asymmetry sequence such that they are too asymmetric for their color. Their asymmetries are not caused solely by star formation, but in part result from tides distorting their structure. (3) Edge-on galaxies also deviate, and generally are too asymmetric or red, both effects caused by dust lanes affecting the morphology (higher asymmetry) and the color (redder).

tried various mathematical schemes to correct A_{90} using A_{180}, simple subtraction worked best. On this basis, we suggest that for statistical purposes the quantity $A_{90} - A_{180}$ be used in place of directly measured axial ratios. This is particularly useful for distorted galaxies without well-ordered, elliptical isophotes; in this case the isophotal measurement of ellipticity is problematic, and A_{90} may prove a useful substitute or diagnostic compared to standard isophotal techniques.

As a result of A_{90}'s sensitivity to the global azimuthal shape of the light profile, A_{90} does not correlate as well with morphological type or color as does A_{180}. For example, at each T-type, there is a larger scatter in the values for A_{90} than for values of A_{180}. A_{90} measured in two different wavebands, R and B for example, do correlate strongly (Fig. 12, both panels). But while A_{90} in the B_J band is a bit more asymmetric, we do not see as strong an increase in the difference between $A(B)_{90} - A(R)_{90}$ as we do for $A(B)_{180} - A(R)_{180}$ (see Fig. 3 and the bottom panel of Fig. 12). We can infer from these observations that A_{90} is not particularly sensitive to the flocculent asymmetry due to star formation that A_{180} most effectively measures. We do note that the dispersions in $A(B) - A(R)$ are about twice as large for A_{90} than for A_{180}. This may be attributed simply to the larger A_{90} values.

It is worth noting that spheroidal systems (elliptical and S0) stand out as never having $A_{90} > 0.70$, which is uncharacteristic of the other T-types. We expect all ellipticals, being largely devoid of star formation, to have A_{180} values ≈ 0 along the entire elliptical sequence from E0 to E7. However, only round elliptical galaxies (E0) would be expected to have zero asymmetry values for any rotation angle ϕ. The more the elliptical deviates from a round shape, the more the value of A_{ϕ} will change as the angle of rotation ϕ changes. Since a measure of A_{90} can give an idea of the shape, the morphology for elliptical galaxies can also be estimated. There is a slight correlation between the Hubble morphological type index for ellipticals [e.g., E6, where $6 = 10(1 - b/a)$] but we do not have enough ellipticals in our sample to say whether A_{90} is useful for determining the Hubble subtype for ellipticals. As is always true for determining elliptical subtype, projection effects are an issue.

It also is interesting to note that there is some scatter in the A_{90} values even for E0s. Either E0s are not completely

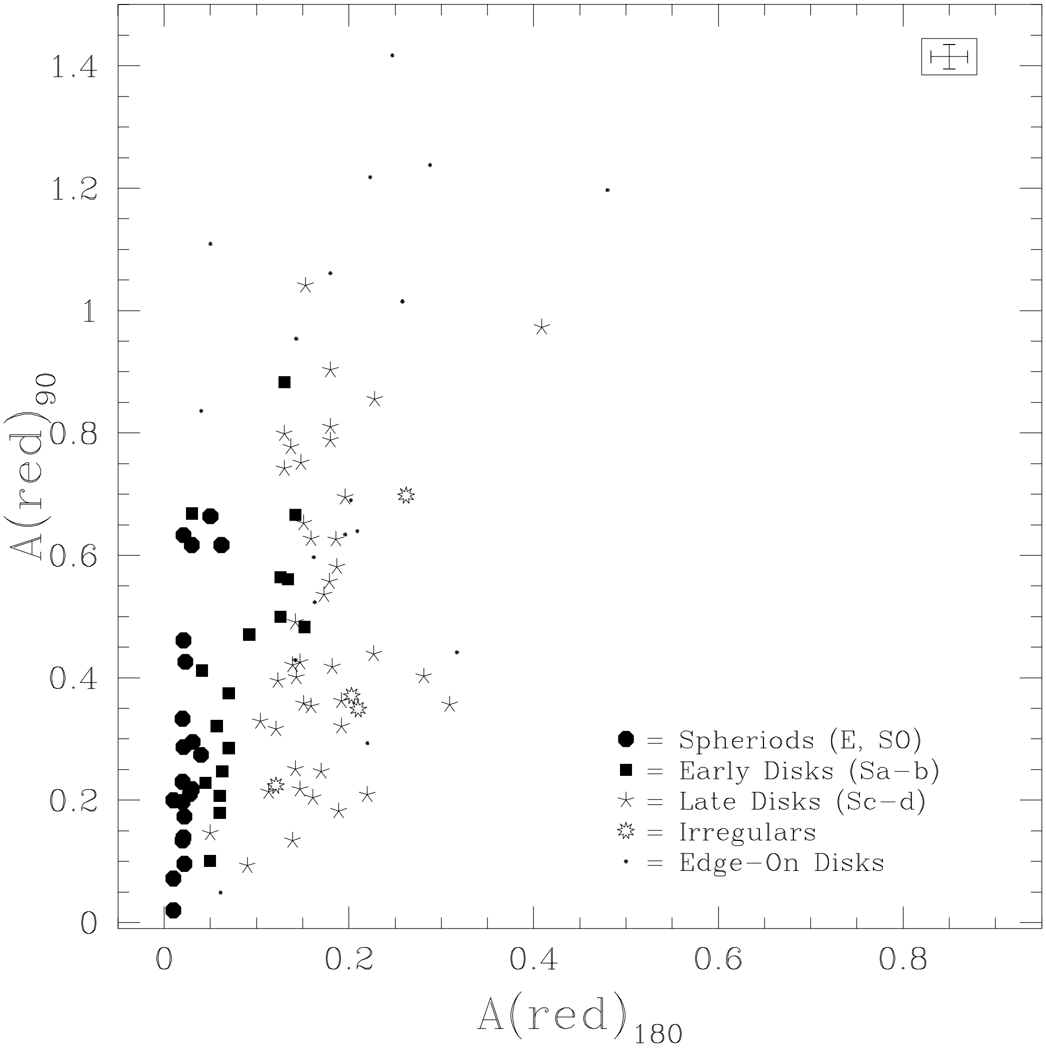

FIG. 11.—Relationship between A_{90} and A_{180}. Plotted here as different symbols are spheriods, early-type disks, late-type disks, irregulars, and edge-on galaxies. For a given range of A_{180} there is a high scatter in the A_{90} values. The edge-on galaxies stand out in this diagram as being the systems with the highest A_{90} values for their A_{180} values. There is also a fairly sharp division between spheriods/early-type disks and late-type disks. We also find no spheriods and few early-type disks with $A_{90} > 0.7$. This type of plot can therefore be used to determine general properties of a sample of galaxies.

round, or they contain a hidden disk structure, as proposed by Kormendy & Bender (1996), to explain the isophotal features of elliptical galaxies.

A final point to note about Figure 11 is the objects with extreme 90° asymmetry values, i.e., $A_{90} > 0.8$ are almost exclusively edge-on systems. Hence by using both A_{180} and A_{90}, these galaxies with high inclinations can be singled out in an automatic process.

4.1.3. *Azimuthal Rotation Profiles*

To test if other angles are instructive as morphological indicators, we have computed the asymmetry index A_ϕ for rotation angles ϕ from 0 to 360° with 1° increments for the 21 galaxy subset representative of the Frei sample defined in § 2. These are displayed in the rightmost columns of Figures 4–7. Naim & Lahav (1997) have also considered a variety of rotation angles in the context of attempting to define galaxy "peculiarity." The treatment here is somewhat more general.

The salient feature of all the asymmetry-rotation angle profiles is the remarkable similarity of the basic shape: the asymmetry profile (which starts at 0 by definition at $\phi = 0°$) rises steeply at first, plateaus near 90°, where there is a maximum, and then descends to a local minimum at 180°. To first order, these profiles are remarkably similar for counterclockwise rotation from $0 < \phi < 180$ and clockwise rotation from $0 > \phi > -180$. In Figures 4–7, the counterclockwise and clockwise rotation profiles through $0 < |\phi| < 180$ are shown as solid and dashed curves, respectively. The fact that dashed curves are frequently not seen reflects this striking similarity. To second order, these profiles are also remarkably similar even about 90° symmetry points, i.e., the curves from $0 < \phi < 90$ and $90 < \phi < 180$ are often indistinguishable except near $\phi = 0$ and $\phi = 180$. The profiles are folded every 90° in Figures 4–7 to illustrate this point. We find, like Kornreich et al. (1998) that most galaxies are symmetric in ϕ.

The location of the local minimum of the asymmetry rotation profile at the 180° has some interesting implications. For example, if a galaxy has a triple- or four-arm pattern, this could be reflected in minima at 120° or 90°, respectively. Previous work on this topic found a significant number of galaxies with triple-arm patterns, revealed by rotations and subtractions similar to what is presented here

(Elmegreen et al. 1992). While one might conclude that such symmetries must be rare, it is more likely that they are simply of lower amplitude than the basic axisymmetry inherent to virtually all galaxies in this sample. This axisymmetry, coupled with projection, determine the primary features in the rotation profiles as described above.

As previously discussed, one may infer that galaxies are axisymmetric at 180° rotation angles because they are dynamically relaxed; axisymmetry is the lowest energy state. Perturbations from this ground state due to recent dynamical events, however, should be revealed in the details of the asymmetry rotation profiles. Indeed, in detail, there are variations in the slope of these profiles at all ϕ. These variations appear to correlate with galaxy type.

For example, there are variations in both the location of the maxima near $\phi = \pm 90$ and local minima near $\phi = \pm 180$. The maxima tend toward smaller ϕ for latter types, qualitatively consistent with the results of Naim & Lahav (1997) for what they describe as increasingly peculiar systems. Likewise, there are a variety of slopes at any given value of ϕ, and many cases where there are subtle variations in the basic 90° symmetry of the rotation profiles. Measurements of the steepness of slope at several fiducials (e.g., 0°, 30°, 60°, and 90°) could reveal interesting correlations with other physical parameters. While these differences could be quite illuminating for the physical understanding and classification of these systems, such an analysis is left for future work.

4.2. *Symmetry as a Function of Galactic Radius*

The asymmetry index is highly sensitive to the aperture size, as illustrated in the third panel of Figures 4–7. The question is, then, what radius should be used? While in principle any radius can be used, one well-defined alternative is to choose a single radius tied to the physical scale of the galaxy. Clearly whatever choice is made, it must be used consistently for comparative purposes. We approached this decision by computing A_{180} first for a wide variety of different, well-defined radii tied to the metric (physical) scale of each galaxy (as described below). We then determined empirically which asymmetry value correlated best with other physical parameters, such as color.

Traditionally, galaxy radii have been defined using a surface brightness criteria, such as the Holmberg radius at $\mu_B = 26.5$ mag arcsec^{-2}. These radii, defined to be at the galaxy isophote where the galaxy is just distinguished from the sky on a particular set of photographic plates, are often inadequate, inappropriate, or ill-defined when trying to compare a wider range of galaxy types at various distances. For example, low surface brightness galaxies pose a particular problem here. The $(1 + z)^{-3}$ surface intensity dimming (detected photons per bandpass), coupled with k-corrections, further makes the definition of an isophotal radius difficult at best, even for normal galaxies. Evolution only adds to the complication in the isophotal approach; and photometric zero points are also of concern. In short, isophotal radii, while operationally convenient to measure, are prone to a wide variety of systematics and therefore are among the least robust measures of galaxy radii.

When establishing a characteristic galaxy size, a radius should be used that is independent of the overall normalization of the surface-brightness distribution, and therefore independent of redshift and photometric calibration. Two possible alternatives to defining radii, θ, are based on (1) the η-function (Petrosian 1976) and (2) the curve of growth, $g(\theta)$. The latter requires a robust, working definition of a total magnitude. Such schemes have been discussed at length elsewhere (e.g., Bershady et al. 1994; Bershady, Lowenthal, & Koo 1998), and here we adopt the protocol developed by Bershady et al. (2000), which uses twice the radius where $\eta = 0.2$ to define the total light.[3] Tables 3 and 4 list the asymmetries computed at the various η and curve-of-growth radii. Based on these measures, we have determined that the radius where $\eta = 0.2$ delivers the best correlation with $B-V$ color. Asymmetries computed with the other radii also show a correlation in color. In principle, any radius can be used, as long as it is consistently used when comparing different galaxies. Occasionally, the $\eta = 0.2$ radius yields extraction regions that extend beyond the image boundaries for the Frei sample. When this occurs, we compute the asymmetry at the largest radius possible.

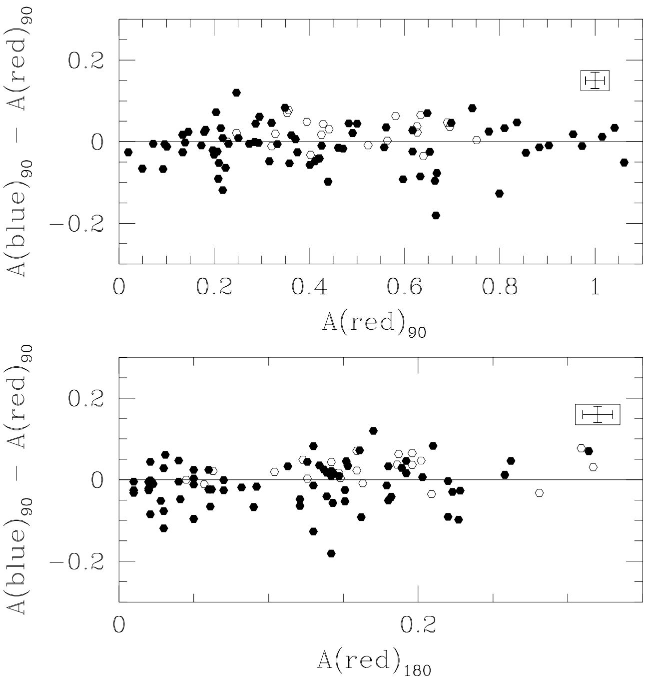

FIG. 12.—Plot of the asymmetries in the R and B bands computed by rotating the galaxy by 90° instead of the nominal 180°. The mean difference $A(B)_{90} - A(R)_{90}$ is near zero for all $A(R)_{90}$, in contrast to $A(B)_{180} - A(R)_{180}$, which systematically deviates to positive values for larger $A(R)_{180}$. Since most galaxies are not perfectly round, A_{90} measures the ellipticity, or deviations in shape from a perfect circle. The edge-on galaxies always have the highest values of A_{90}. The consistency between the two different wavelengths indicates that contributions to A_{90} are mostly due to global shape. However, higher values are $A(B)$, compared with $A(R)$, and are seen only at the largest values of A_{180}, indicating that star formation is not a significant addition to A_{90}, but does somewhat contribute as expected.

The trend of asymmetry versus aperture radius is useful to determine where sources of asymmetry in a galaxy are coming from, e.g., different relative amounts of nuclear and disk star formation, or low-frequency assymetric structures such as off-center bars and oval disks. It is immediately obvious from inspection of Figures 4–7 that for no galaxy is the asymmetry a constant function of radius. This shows the

---

[3] We follow Kron's (1995) suggestion to use the inverted form of $\eta(r) \equiv I(r)/\langle I(r)\rangle$, which equals 1 at the center of the galaxy and approaches 0 at large galactic radii, r.

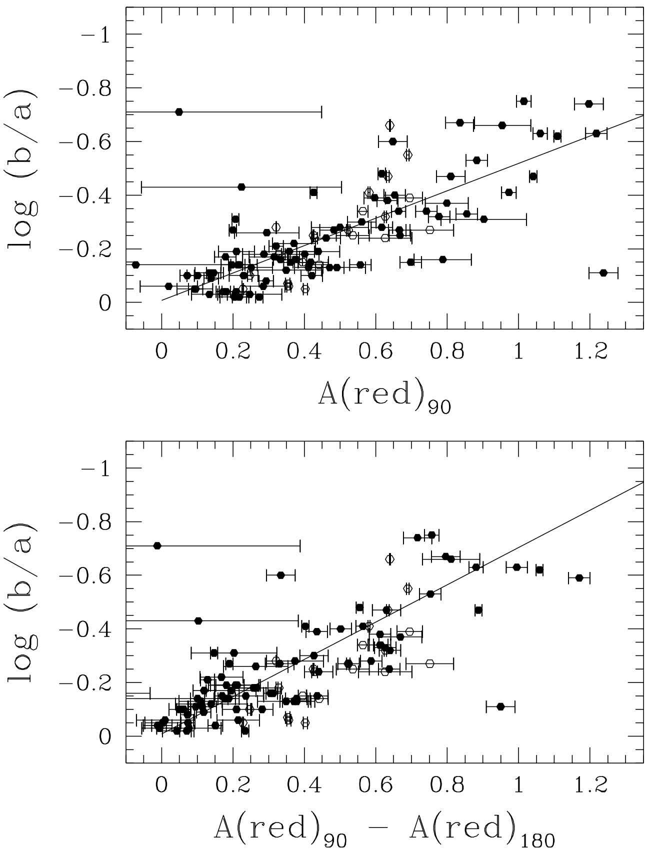

FIG. 13.—Plot of the axis ratio for our sample [log(*b*/*a*) from RC3] vs. the asymmetry computed with a rotation angle of 90°. This strong correlation is evidence that A_{90} is primarily a measure of the azimuthal shape of a galaxy, rather than physical effects such as star formation or dynamical effects that primarily cause A_{180} asymmetries. The bottom plot shows $A_{90} - A_{180}$ plotted instead of A_{90} showing a better correlation, indicating that there is some flocculent asymmetry contributing to A_{90}. Linear regressions are for illustrative purposes.

importance of using a standard radius to compute the asymmetry for a galaxy.

We are able to make a few general observations about the distribution of asymmetric light in a galaxy, which is clearly a function of T-type. Ellipticals and S0s look very similar, with their asymmetry peaking at very low radii, and modestly decreasing outward, and then increasing rapidly at high very large radii (Fig. 4). The central peak may be due to structures commonly found in the centers of ellipticals (Lauer et al. 1995). The sharp rise in asymmetry at large radii is not necessarily a physical effect, but is a result of the noise correction in a regime where the noise dominates the signal.

In contrast, spiral galaxies (Figs. 5 and 6) show an increase in asymmetry with radius, sometimes with local or global maxima at intermediate radii. For the early disks (Sa–b, Fig. 5), the maximum is usually at or near the half-light radii. The late-type disks (Sc–d, Fig. 6) have their peak asymmetry values at higher radii, usually beyond the half-light radii. The irregulars (Fig. 7) also show a remarkable increase in asymmetry as a function of radius, with the inner parts comparatively symmetric.

Maxima in the asymmetry as a function of radius diagrams (Figs. 5 and 6) for disk systems are typically at the locations of H II regions or dust lanes in spiral arms.

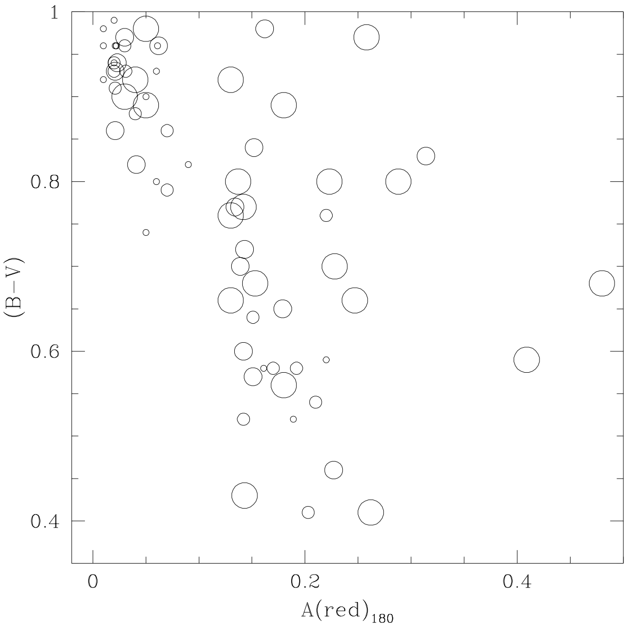

FIG. 14.—Color-asymmetry diagram showing the distribution of galaxies with high axis ratios (*b*/*a*). Principle causes of the scatter in the normal galaxy sequence of Fig. 10 are reddening and morphological changes that occur for inclined galaxies. The galaxies with the highest inclinations are the ones that deviate the most from this sequence.

To summarize the observed trends: as galaxies become systematically later in type, the amplitude of asymmetry increases and the increase with radius becomes stronger. That is, the latest type galaxies are pronouncedly more asymmetric in their outer parts than in their inner parts compared to earlier-type galaxies. This characteristic could, in principle, be an objective method for determining a galaxy's Hubble type. One physical explanation for this trend of larger radii peaks in asymmetries for later types is the increasing dominance of actively star-forming disks in late-type systems. However, other possibilities include increasing specific star formation rates with galactocentric radius (Hodge & Kennicutt 1983; Ferguson et al. 1998), the late-time accretion of material in the outer disk with a dynamical-relaxed core (e.g., as proposed by Rix & Zaritsky 1995), or tidal interactions with nearby galaxies. These effects, however, would have to be correlated with morphological type.

A more sensitive probe of the physical cause of these radial trends in asymmetry would be to examine the rotational asymmetry in annuli and to compare the specific asymmetry, as measured in these annuli, to the specific color of the annuli. As we have argued above, a significant component of the color-asymmetry correlation is due to what we have termed flocculent asymmetry, i.e., the irregular distribution of H II regions in an otherwise axisymmetric system. However we have also noted that departures from the color-asymmetry trend for normal galaxies appears to be an indication of larger scale asymmetry; what we refer to as dynamical asymmetry. These statements describe the relation between the integrated asymmetry and color of galaxies. In analogy, departures from the color-asymmetry trend in a given annulus might help disentangle where and when a galaxy's asymmetry is dominated by star formation or large-scale dynamical asymmetries. The analysis of Kornreich et al. (1998), by excluding the inner portion of the

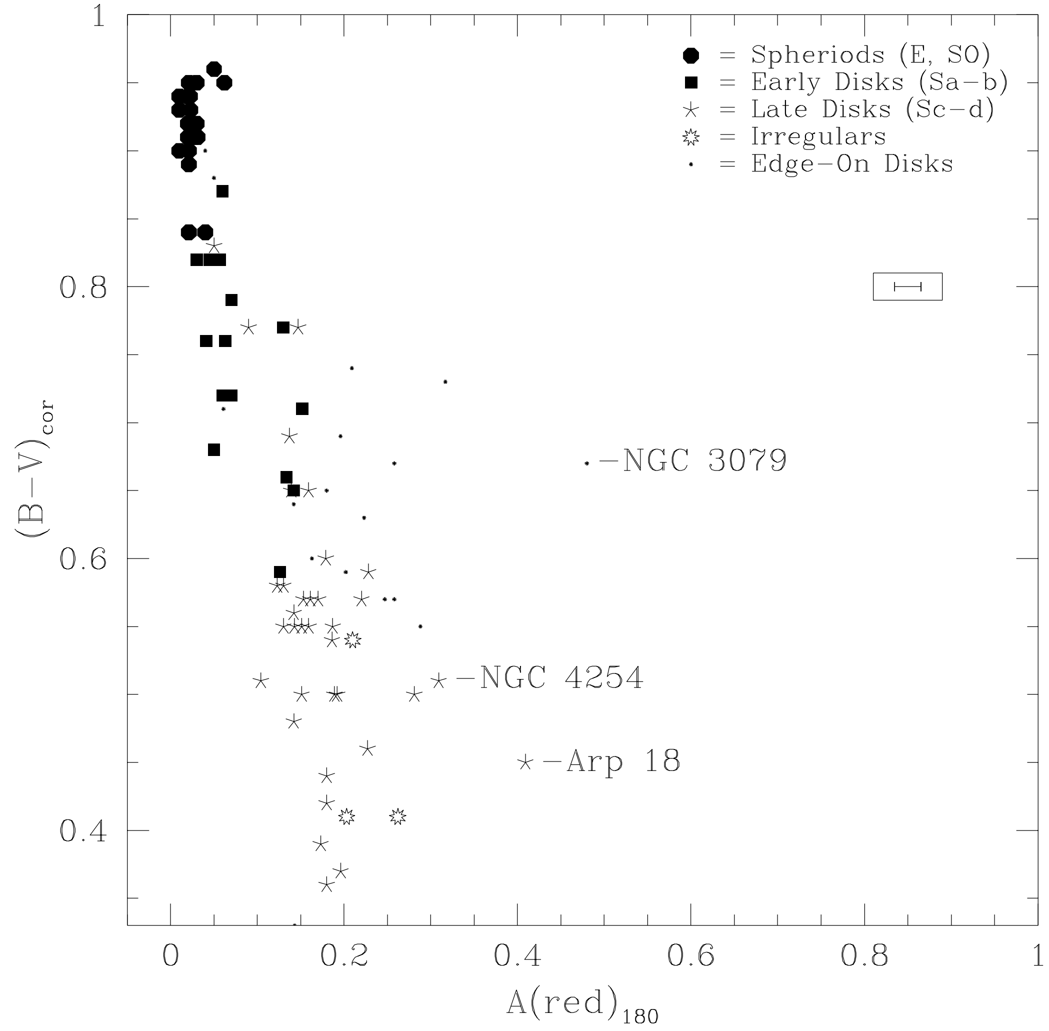

FIG. 15.—Color-corrected color-asymmetry diagram. This version of the color-asymmetry diagram uses dereddened $B-V$ colors, corrected for inclination effects (de Vaucouleurs et al. 1991). The normal galaxy sequence is tighter, and many of the edge-on galaxies nearly coincide with other galaxies having similar colors and asymmetries. This Figure and Fig. 14 show how this diagram is being affected by inclination.

galaxy, achieves this goal. Using rotation instead of a modal analysis, and adding more radial resolution would offer further dimension to this study, and we will pursue this elsewhere.

4.3. *The Correlation of Color and Asymmetry*

The color-symmetry diagram is a powerful tool that can be used for both morphological and physical differentiations of galaxies, and hence can be used as a diagnostic for understanding distant galaxies, and galaxy evolution (C97; Conselice & Bershady 1999). The color-asymmetry diagram (Fig. 10), when using only the normal face on galaxies presents a tight, linear sequence, as shown in C97. This normal-galaxy sequence represents a lower limit where, for any given asymmetry, there are no galaxies with bluer colors; we refer to this as the "fiducial" galaxy color-asymmetry sequence.

When the entire Frei sample is included (with normal, active, edge-on, irregular, and peculiar galaxies), still no galaxies are seen to occupy the symmetric-blue region (Fig. 10, *bottom left*). This shows that blue galaxies—at least in the Frei et al. sample—are asymmetric galaxies. Symmetric blue galaxies may exist, however, at higher redshift (e.g., Schade et al. 1995).

To first order, the color-asymmetry diagram of Figure 10 gives a wealth of diagnostic information for classifying galaxies of different morphologies. The elliptical and spirals separate distinctly in this diagram. Ellipticals, denoted as large circles, are always found at the upper left portion of the diagram where red and symmetric objects are located. Edge-on systems, located by tiny dots, occupy the space to the right of the diagram. The spirals and irregular galaxies, plotted as boxes (early types Sa–b), stars (later types Sc–d), and open circles (irregulars), are always bluer and more asymmetric than the ellipticals. In short, the late-type versus early-type galaxies can clearly be differentiated in an automatic method via the color-asymmetry diagram.

In addition, the color-asymmetry diagram presents the possibility to single out galaxies undergoing an interaction or merger. In Figure 10, we have labeled the galaxies that are most likely undergoing an interaction with another galaxy or are otherwise peculiar. These objects stand out as being too asymmetric for their colors, therefore star formation cannot be the only cause of the asymmetry as it is for the galaxies on the fiducial sequence. Of the three galaxies labeled, all are Sc–d systems. NGC 4088 (Arp 18) has an outer arm receding and an elongated nucleus (Vorontsov-Velyaminov 1977; Dahari 1985), which is possible evidence for a recent tidal interaction. NGC 4254 is a Virgo Cluster spiral that is thought to have an external driving mechanism (Rauscher 1995), which is possibly a result of tidal interactions with the core of the Virgo Cluster. One of its arms is overly extended and asymmetric. NGC 3079 is an edge-on galaxy with evidence of a warp. These are the only galaxies in the Frei sample that have evidence for interactions, and they all can be distinguished by examining their place in the color-asymmetry diagram. Other galaxies that have colors similar to interacting galaxies (such as the Magellanic irregular NGC 4449, as its asymmetry is caused by star formation) fall closer to the fiducial sequence (Fig. 10). When applied to images of distant galaxies, this segregation can be used as an effective tool for disentangling possible evolutionary effects, e.g., the role of mergers and interactions as opposed to star formation.

The edge-on galaxy systems stand out in Figure 10 as objects that are too asymmetric for their colors. However, they generally are not as asymmetric as the interacting galaxies, and have redder colors. Indeed, a large portion of the scatter of the galaxies in the color-asymmetry diagram can be accounted for by this inclination, as demonstrated in Figure 14. Here the color-asymmetry diagram is revisited but with galaxies of higher inclinations labeled with larger symbols. (The four sizes represent quartile bins in the observed R-band A_{90} distribution.) The galaxies that contribute to the scatter the most are also the most inclined, almost without exception. As one might infer from the tight correlation in Figure 13, one reaches the same conclusion marking sources according to axis ratio instead of A_{90}. This raises the possibility that the scatter could be reduced with a hybrid asymmetry-color diagram that included or corrected for inclination.

Since inclination potentially can affect both the apparent asymmetry and color, a first step is to determine how each of these parameters is being affected. That galaxies become redder with increasing inclination is of little doubt, yet the behavior of asymmetry with inclination is less obvious. When we plot the color-asymmetry diagram using colors corrected for extinction (de Vaucouleurs 1991), the scatter is dramatically reduced as seen in Figure 15. From this exercise one may conclude that the effects of inclination on asymmetry are, in comparison to color, second order.

While inclination-corrected colors yield a stronger asymmetry-color relation, ideally we would like a method of correcting for inclination that is robust over a range of distance. Our concern is that the inclination corrections of de Vaucouleurs (1991) represent an excellent, but fine-tuned

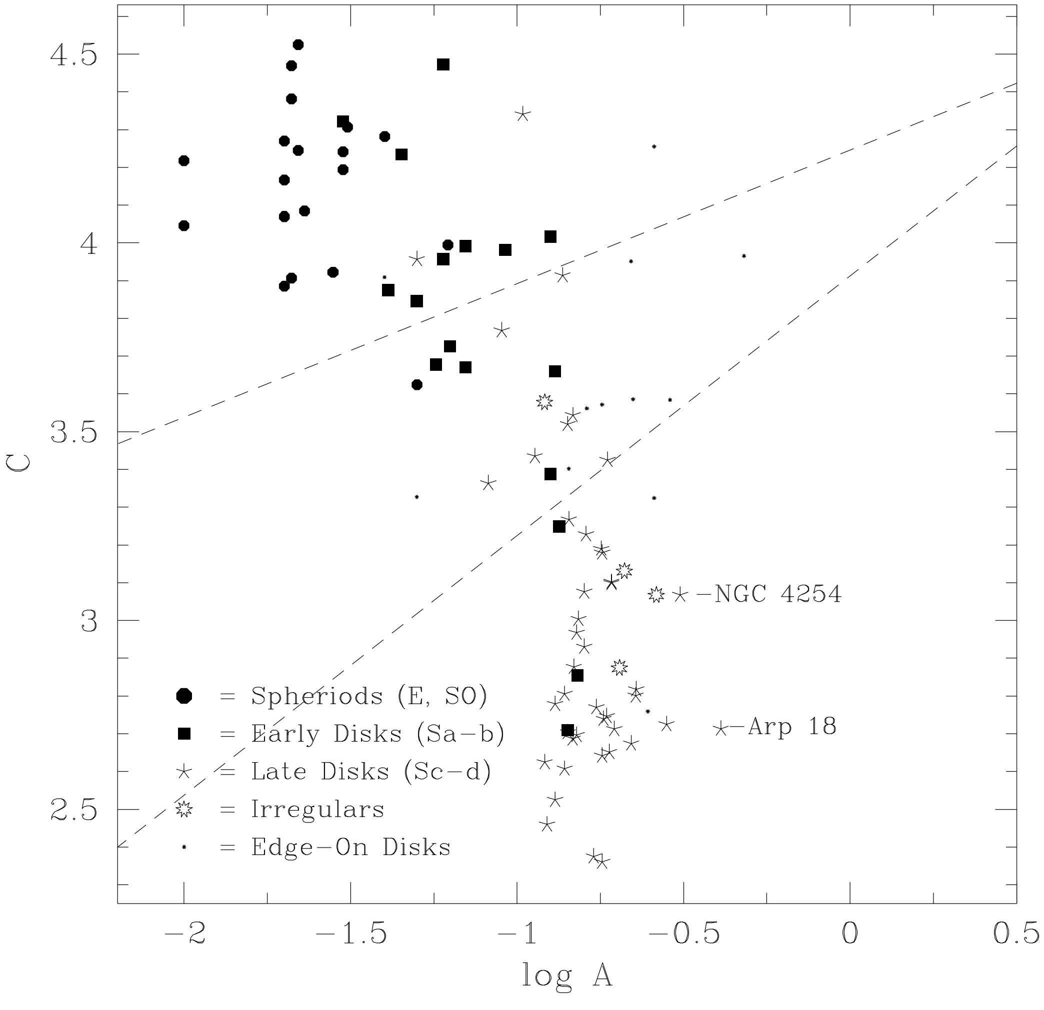

FIG. 16.—Asymmetry-concentration diagram. This diagram is similar to the one used by Abraham et al. (1996b) for galaxies in the Hubble Deep Field. The spheriods stand out in this diagram as being the symmetric and most concentrated objects, while the late disks are less concentrated and more asymmetric. There is not, however, as clean a division between early and late disks as seen in the color-asymmetry diagram (Fig. 12). Interestingly, nearly all of the edge-on disks fit between the two dashed lines.

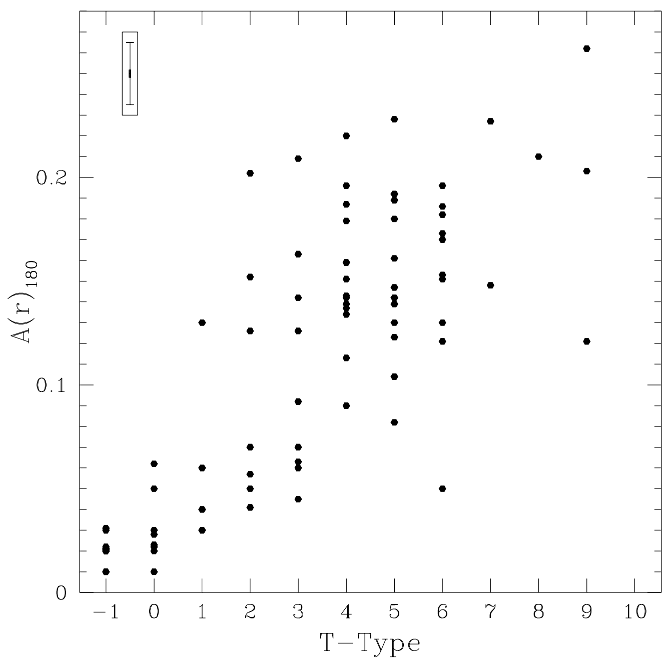

FIG. 17.—Asymmetry distribution as a function of Hubble T-type. There is a general increase in average asymmetry at later types, but there is a large scatter in asymmetry at each Hubble type, similar to the pattern found for most physical parameters.

algorithm based on large, normal galaxies, and require an accurate identification of a galaxy's T-type and b/a at a rest-frame isophote comparable to what is used locally. We already have discussed at length the problems of basing measurements on isophotes. Our hope is that A_{90} may offer a more robust substitute. However, examining correlations of the residuals about the observed color-asymmetry relation with A_{90}, for example, there is no simple empirical way to correct these residuals. This is obvious from a more careful inspection of Figure 14: while it is true that most of the outliers from the fiducial sequence have large A_{90}, a good number of galaxies with large A_{90} also lie in this fiducial sequence. We suspect that more information about type (possibly by using light concentration) may allow us to achieve a better inclination correction. To develop this possibility requires a larger training sample and will be explored in a future paper.

4.4. *The Correlation of Asymmetry with Other Morphological and Physical Parameters*

4.4.1. *Asymmetry and Image Concentration*

There is also a correlation between asymmetry (A) and the concentration (C) of light for galaxies, as first found by A96, and revisited here in Figure 16 using new measurement algorithms. The concentration index is from Bershady et al. (2000), and is defined as the logarithm of the ratio of the radii enclosing 20% and 80% of the light. In principle, this diagram could be used for the same classification purposes as color and asymmetry. It could be argued that asymmetry and image concentration are methodologically superior since, unlike color, measures of both asymmetry and concentration do not require knowledge of the source redshift (at least to first order). However, as discussed by Bershady et al. (2000), there are substantial dependencies of these image structural parameters on redshift that must be corrected, thereby mitigating their putative advantage. Our A-C diagram, which has a tighter correlation than A96, is as tight as A-color. One difference is that the A-C is double valued. Nonetheless, this can be handled with an affine parameter, as A96 has effectively done. An advantage that A-C has over A-color is that the edge-on galaxies do not appear to have a substantially different distribution. This is another indication that A is only weakly affected by inclination.

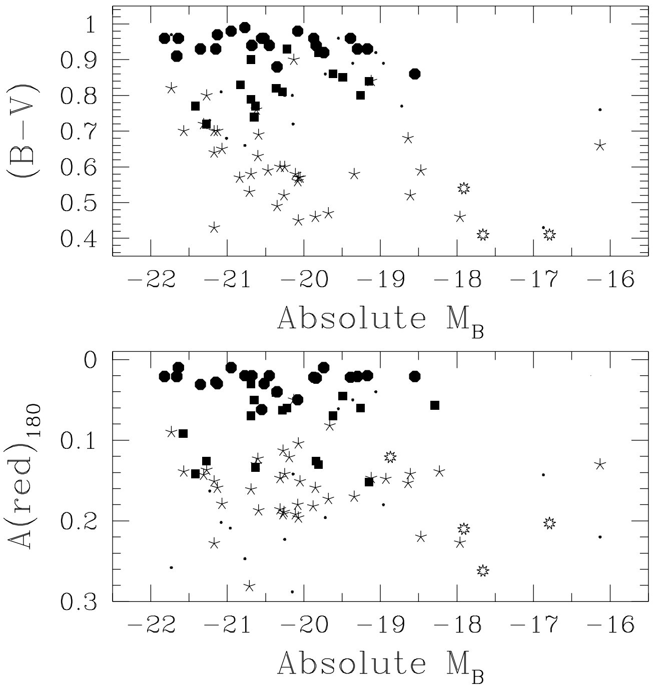

FIG. 18.—*Top*: $B-V$ vs. B absolute magnitude, with different symbols distinguishing morphological types as in Fig. 16. *Bottom*: Red asymmetry parameter (R or r) plotted as a function of the absolute magnitude. As shown in Conselice (1997) there is little correlation between the intrinsic brightness and asymmetry of a galaxy for the narrow range of magnitudes in the Frei et al. sample.

4.4.2. *Asymmetry, T-type, and Luminosity*

As was shown in C97, the asymmetry value for a galaxy correlates with T-type. For the larger sample used in this paper, the asymmetry–T-type plot is shown in Figure 17 with a similar result, namely, that the Hubble sequence is one of increasing asymmetry with a substantial scatter.

Conselice (1997) also showed that asymmetry does not correlate strongly with absolute magnitude, illustrated here in the bottom panel of Figure 18 for the larger sample. One might expect such a correlation since color-luminosity relations are known to exist for all galaxies even in the optical (Huchra 1977; Bershady 1995), and color and asymmetry are tightly correlated. However, we note that given the limited dynamic range in luminosity of this sample, the lack of a strong correlation between asymmetry and luminosity is not surprising. For example, the color-luminosity correlation exhibited by this sample is paltry for this reason, as illustrated in Figure 18*a*.

When we test the relationship between the asymmetry parameters and the van den Bergh luminosity classification (van den Bergh 1960a, 1960b) for the subsample with known van den Bergh luminosity types, we again do not see

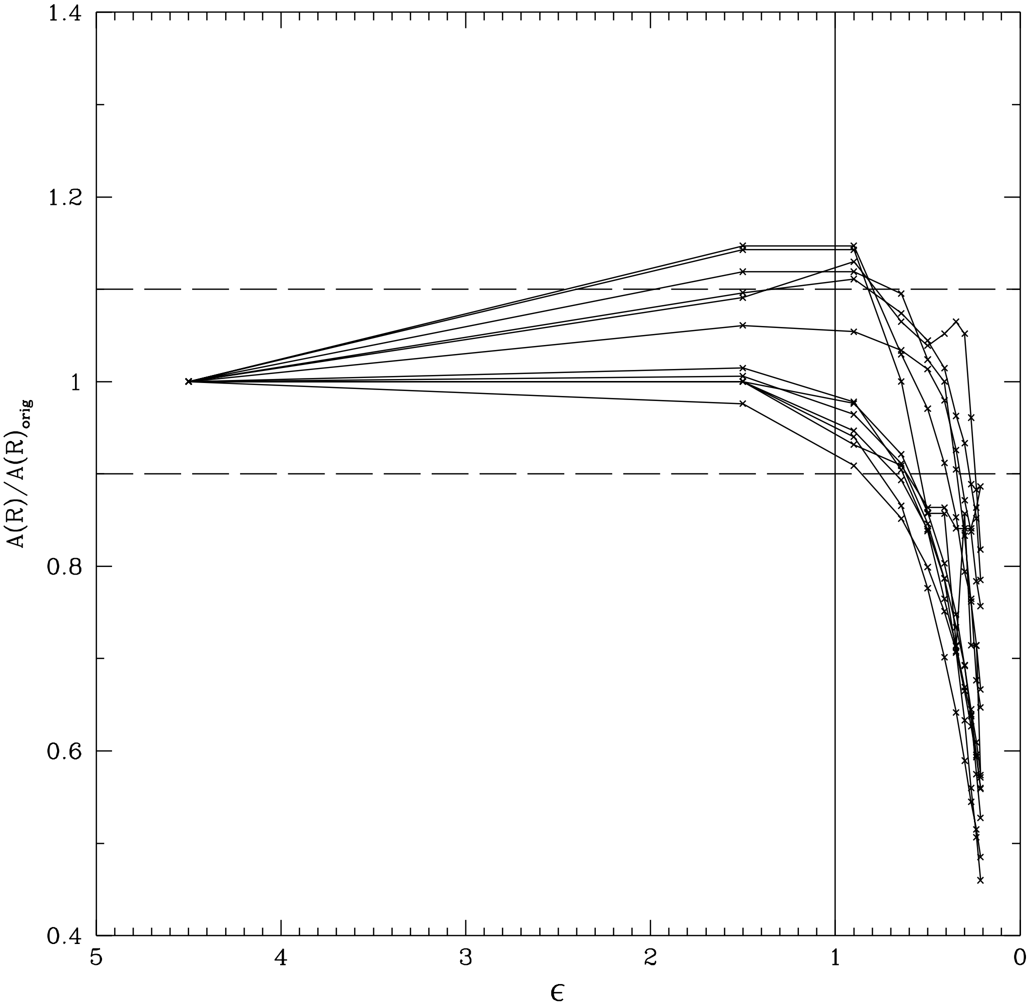

FIG. 19.—Asymmetry as a function of spatial resolution. The parameter ϵ is the ratio of the angular diameter corresponding to 0.5 h_{75}^{-1} kpc divided by the angular resolution. From this plot it can be seen that the asymmetry of a galaxy is measurable to better than 10% down to $\epsilon \approx 1$.

a correlation between these two morphological parameters. This suggests that asymmetry is a perpendicular morphological parameter to the luminosity class of a galaxy. A detailed system of morphology using the T-type, asymmetry, and luminosity class of a galaxy is possible, and will be the subject of a separate paper.

5. APPLICATION TO DISTANT GALAXIES

In § 3.4 we established that asymmetry can be well-measured for $S/N \geq 100$ (within the half-light radius). Here we determine the other most relevant observational parameter: the required spatial resolution for accurate asymmetry measurements. For this purpose, we define ϵ as the ratio of the angular diameter subtending 0.5 h_{75}^{-1} kpc at a given distance ($\theta_{0.5\,{\rm kpc}}$, where $h_{75}^{-1} = H_0/75$ km s^{-1} Mpc^{-1}) to the angular resolution of the image ($\theta_{\rm res}$):

$$\epsilon \equiv \frac{\theta_{0.5\,{\rm kpc}}}{\theta_{\rm res}} .$$

The choice of numerator stems from the results of our simulations, which, as we will discuss, show the asymmetry parameter was found to be recoverable when the resolution element was greater than 0.5 h_{75}^{-1} kpc. Hence ϵ provides an index of the resolving power of a telescope relevant to the measurement of a galaxy's asymmetry.

For subjective morphological classifications such as the classical Hubble scheme, as one might expect, as long as a galaxy's large-scale structure (e.g., the bulge and disk components) can be resolved, at least a rudimentary classification can be given. For large galaxies, one might estimate that ∼1 kpc physical resolution is marginally adequate, i.e., $\epsilon \sim 0.5$. This resolution is afforded by *HST* essentially at all redshifts. However, since the appearance of the spiral arms and the flocculence of the disk is important in the Hubble classification, higher spatial resolution ($\epsilon \geq 1$) is required to make classifications comparable to what is done for nearby galaxies even from ground-based images. Nonetheless, the Hubble scheme has been used to classify distant galaxies as seen in moderate to deep *HST* images (van den Bergh et al. 1996), and has been automated using neural networks (e.g., Odewahn et al. 1996).

Since a critical component of asymmetry in normal galaxies also is due to flocculence, then there could be substantial systematics of the observed asymmetry with resolution (distance). In C97, a slight distance effect was seen: the value of the asymmetry parameter (A) was found to decrease very slightly with increasing distance, i.e., the sources appeared to become more symmetric. We find a similar type of relationship using the entire Frei sample, where galaxies on average become more symmetric at higher distances. Mitigating this effect is that the most distant sources in

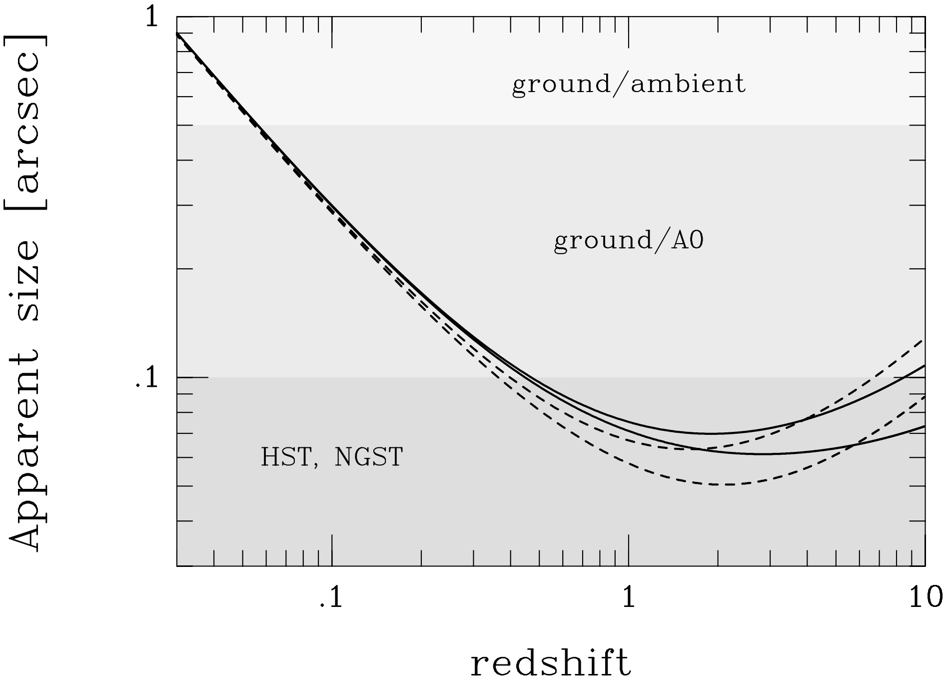

FIG. 20.—Apparent size vs. redshift for a metric length of 0.5 h_{75}^{-1} kpc and several values of Ω composed of nonrelativistic matter and a cosmological constant. The solid lines are for $\Omega_{\rm total} = 0.1$ and 0.3, and $\Omega_\Lambda = 0$; i.e., $q_0 = 0.05$ (*bottom solid lines*) and 0.15 (*top solid lines*). The dashed curves are for $\Omega_{\rm total} = 1$, with $\Omega_\Lambda = 0.9$ and 0.3; i.e., $q_0 = -0.850$ (*bottom dashed lines*) and -0.550 (*top dashed lines*). Accessible apparent sizes for different instrument classes are indicated by the shading: modern ground-based telescopes at good sites in ambient conditions (ground/ambient, e.g., WIYN); ground-based telescopes with adaptive optics (ground/AO, e.g., Canada-France-Hawaii-Telescope); and space-based telescopes (*HST*, NGST). Since scales of 0.5 h_{75}^{-1} Mpc must be resolved to accurately measure rotational asymmetries, cosmological measurements of asymmetry require spatial resolutions of 0".1 or better.

our sample tend to be red, and thus have lower intrinsic asymmetry.

To determine the importance of image resolution on the measured asymmetry, we simulated the appearance of the Frei et al. galaxy sample, as they would be observed at large distances with, e.g., *HST*. The simulations are simple in that we considered only the change in apparent size relative to a fixed apparent pixel size. The effects of image blur and redshift (i.e., change in observed portion of the galaxy rest-frame spectrum) were ignored. In other words, we assume here that the point-spread function (PSF) abberations are small compared to the pixel size, and that the observed bandpass is shifted with redshift, respectively. Both of these assumptions are reasonable for substantial data sets combining multiband images using the *HST* Wide-Field Camera 2.

The sources in the simulated degraded images had their asymmetry computed by the same method described in § 3. The centering algorithm is particularly important here. For less well-resolved sources the relative error in selection of an image can be large. We observed that the mean and mode of the light distribution changed significantly at the pixel level as galaxy's image was sampled more coarsely, even though the original images of most galaxies had a visually well-defined center.

However, even using our routines that find the minimum asymmetry, we find that almost all galaxies decrease in their asymmetry value when artificially degraded, as shown in Figure 19. Interestingly, we find that the most symmetric galaxies (ellipticals) have asymmetries that initially increase at coarser sampling redshifts, an effect also noticed by Wu, Faber, & Lauer (1997). Recall that the higher the value of ϵ, the better a galaxy is spatially resolved and sampled. As ϵ decreases, so too does the asymmetry parameter. However, while the asymmetry parameter does decrease in Figure 19, the ϵ-values change by a factor of 20; for $\epsilon > 1$, the measured asymmetries remain close to the high ϵ-value.

Fortunately, the angular size of a galaxy changes little beyond $z \sim 0.7$ for a wide range of cosmologies. At $z = 1.25$, a galaxy observed in the HDF, where $\theta_{\rm res} \sim 0.045$, will have $\epsilon \sim 1.3$ ($q_0 = 0.5$, $\Lambda = 0$), and greater at higher and lower redshifts for this cosmology. In comparison, a typical Frei et al. sample galaxy has a size of about 4′, with a pixel size of 1".35, with $\epsilon = 5$. These ϵ values are both in a range where asymmetry changes little with ϵ, hence their asymmetries can be reliably compared. We nominally confirm, then, the results of A96 that resolution degradation of asymmetry for distant galaxies observed with *HST* is not a significant effect if the highest available resolutions are obtained. We note, however, that ϵ for distant galaxies in the HDF is just on the edge of being acceptable for asymmetry measurements. For $q_0 < 0.5$ ϵ remains above 1, but for coarser pixel sampling ϵ quickly falls below 1, an issue particularly germane to near-infrared camera and multiobject spectrometer (NICMOS) imaging data unless it is properly over sampled.

Our computations of how the angular diameter will change as a function of redshift, illustrated in Figure 20, shows that galaxies at any redshift imaged with the *HST* can have their asymmetries reliably computed with the suitable instrument. Even with excellent seeing on ground-based telescopes (e.g., WIYN 3.5 m telescope in 0".6 seeing), asymmetry measurements can only be computed reliably out to $z \approx 0.1$. This shows the importance of instruments like *HST* and the *NGST* for morphological studies of high-redshift galaxies. Similarly, high-order adaptive optics on large ground-based telescopes will permit asymmetry measurements at large distances.

A caveat worth noting is that our simulations are based only on large, luminous galaxies. There exists the possibility that physically small galaxies have a systematically different power spectrum of luminosity fluctuations due to a scale dependence on the number of large star-forming sites (Elmegreen & Efremov 1996). If so, our prescription based on a single ϵ index may be overly simplistic.

6. CONCLUSIONS

We described the use of the 180° rotational asymmetry parameter for both physical and morphological diagnostic uses and placed its computation on a firm basis to allow comparisons between nearby and high-redshift galaxies. We tested several methods of computing rotational asymmetry, concluding that a substantially modified version of Abraham et al.'s (1996a) method correlated best with physical parameters such as color. The three critical modifications that we have developed here include (1) an unambiguous and robust definition of a center of rotation; (2) a new method for correcting for noise that uses the same minimization method that is independently applied to the source; and (3) a well-defined radius within which asymmetry is measured. We artificially redshift galaxies to determine the dependence of our asymmetry measure on resolution and S/N asymmetry measurements. As expected, distance affects a galaxy's asymmetry measurement by making the galaxy more symmetric. With this revised rotational asymmetry algorithm, we estimated via simulations that asymmetry can be robustly measured down to an integrated S/N of 100 (as measured within the half-light radius), and with spatial resolution above 0.5 h_{75}^{-1} kpc.

We also investigated the asymmetries computed as a function of the rotation angle, ϕ, finding a strong minimum in asymmetries at a rotation angle of 180°, and maxima near 90°. To first order, these asymmetry rotation profiles are remarkably similar from galaxy to galaxy. To higher order, variations in these profiles undoubtedly offer further information for probing the light distributions of galaxies. We also find different behavior in the asymmetry of a galaxy as a function of its radius. Elliptical galaxies have a modest decline in asymmetry with increasing radius, while later-type galaxies have a pronounced, opposite trend.

We also found that 180° asymmetries correlate well with Hubble morphological type, color, and concentration. We suggested that the color-asymmetry relation for galaxies is a fundamental one that can be exploited in several different ways to obtain information about galaxies. From the color-asymmetry diagram alone, we were able to distinguish between spirals, ellipticals, and edge-on galaxies, as well as interacting galaxies. The 90° asymmetries correlate strongly with ellipticity (b/a), and can be used to tighten further the correlation of color to asymmetry.

We found no correlation between the absolute magnitude or van den Bergh (1960a, 1960b) luminosity class and the asymmetry parameter of a galaxy. Asymmetry, which appears to be closely related to color (and therefore the relative youth of a galaxy's stellar population), appears to be a morphological indicator perpendicular to this luminosity class. While the degree of asymmetry represents an indicator roughly parallel to the Hubble sequence, our expectation is that asymmetry can be used in conjunction with other quantitative parameters to develop a new, refined morphological classification. Such a classification would have a more directly interpretable physical basis, but need not—indeed, should not—be forced to duplicate the Hubble sequence.

We thank Greg Wirth for several stimulating conversations on computing asymmetry in a nonbiased way. Both C. J. C. and M. A .B. thank Richard G. Kron for his ideas on galaxy morphology, the Hubble sequence, and for his encouragement over the years. We thank the referee, Roberto Abraham for his thorough reading of the manuscript and for useful comments that improved the presentation of this paper. This research was supported by NASA LTSA grant NAG5-6043, STScI grants AR-7518 and GO-7875, and research funds from the University of Wisconsin graduate school (M. A. B.). Space Telescope Science Institute (STScI) is operated by Association of Universities for Research in Astronomy, Inc., under NASA contract NAS5-26555. C. J. C. acknowledges the hospitality of Mark Dickinson and STScI, where part of this work was completed.

REFERENCES

Abraham, R. G., van den Bergh, S., Glazebrook, K. Ellis, R. S., Santiago, B. X., Surma, P., & Griffiths, R. E. 1996a, ApJS, 107, 1 (A96)

Abraham, R. G., Tanvir, N. R., Santiago, B. X., Ellis, R. S., Glazebrook, K., & van den Bergh, S. 1996b, MNRAS, 279, L47

Abraham, R. G., Valdes, F., Yee, H. K. C., & van den Bergh, S. 1994, ApJ, 432, 75

Baldwin, J. E., Lynden-Bell, D., & Sancisi, R. 1980, MNRAS, 193, 313

Bershady, M. A. 1995, AJ, 109, 87

Bershady, M. A., Hereld, M., Kron, R. G., Koo, D. C., Munn, J. A., & Majewski, S. R. 1994, AJ, 108, 870

Bershady, M. A., Jangren, A., & Conselice, C. J. 2000, AJ, submitted

Bershady, M. A., Lowenthal, J., & Koo, D. C. 1998, ApJ, 505, 50

Bromley, B. C., Press, W. H., Huan, L., & Krishner, R. P. 1998, ApJ, 505, 25

Burda, P., & Feitzinger, J. V. 1992, A&A, 261, 697

Connolly, A. J., Szalay, A. S., Bershady, M. A., Kinney, A. L., & Calzetti, D. 1995, AJ, 110, 1071

Conselice, C. J. PASP, 1997, 109, 1251 (C97)

Conselice, C. J., & Bershady, M. A. 1999, in After the Dark Ages, When Galaxies Were Young: $2 < z < 5$, ed. S. Holt (College Park: Univ. Maryland Press), 225

Curtis, H. 1918, Publ. Lick Obs., 13, 12

Dahari, O. 1985, ApJS, 57, 643

de Vaucouleurs, G. 1959, Handbook Phys., 53, 311

de Vaucouleurs, G., de Vaucouleurs, A., Corwin, H. G., Buta, R. J., Paturel, G., & Fouqué, P. 1991, Third Reference Catalog of Bright Galaxies (New York: Springer) (RC3)

Doi, M., Fukugita, M., & Okamura, S. 1993, MNRAS, 264, 832

Dressler, A., & Gunn, J. E. 1992, ApJS, 78, 1

Elmegreen, B .G., & Efremov, Y. N. 1996, ApJ, 466, 802

Elmegreen, B. G., Elmegreen, D. M., & Montenegro, L. 1992, ApJS, 79, 37

Elmegreen, D. M., & Elmegreen, B. G. 1982, MNRAS, 201, 1021

Ferguson, A. M. N., Wyse, R .G., Gallagher, J. S., & Hunter, D. A. 1998, ApJ, 506, L19

Folkes, S. R., Lahav, O., & Maddox, S. J. 1996, MNRAS, 283, 651

Frei, Z., Guhathakurta, P., Gunn, J. E., & Tyson, J. A. 1996, AJ, 111, 1

Gullixon, C. A., Boeshaar, P. C., Tyson, J. A., & Seitzer, P. 1995, ApJS, 99, 281

Han, M. 1995, ApJ, 442, 504

Hodge, P. W., & Kennicutt, R. C., Jr. 1983, ApJ, 267, 563

Hubble, E. P. 1926, ApJ, 64, 321

———. 1936, The Realm of the Nebulae (New Haven: Yale Univ. Press)

Huchra, J. P. 1977, ApJS, 35, 171

Kornreich, D. A., Haynes, M. P., & Lovelace, R. V. E. 1998, AJ, 116, 2154

Koopmann, R. A., & Kenney, J. D. P. 1998, ApJ, 497, L75

Kormendy, J., & Bender, R. 1996, ApJ, 464, L119

Kron, R. G. 1995, in The Deep Universe, Saas-Fee Advanced Course 23 (New York: Springer), 233

Lauer, T. R., et al. 1995, AJ, 110, 2622

Martin, P., & Friedli, D. 1997, A&A, 326, 449

Morgan, W. W. 1958, PASP, 70, 364

———. 1959, PASP, 71, 394

Naim, A., & Lahav, O. 1997, MNRAS, 286, 969

Naim, A., Lahav, O., Sodre L., Jr., & Storrie-Lombardi, M. C. 1995, MNRAS, 275, 567
Odewahn, S. C. 1995, PASP, 107, 770
Odewahn, S. C., Windhorst, R. A., Driver, S. P., & Keel, W. C. 1996, ApJ, 472, L13
Okamura, S., Kodaira, K., & Watanabe, M. 1984, ApJ, 280, 7
Petrosian, V. 1976, ApJ, 209, L1
Rauscher, B. J. 1995, AJ, 109, 1608
Richter, O.-G., & Sancisi, R. 1994, A&A, 290, L9
Rix, H.-W., & Zaritsky, D. 1995, ApJ, 447, 82
Ronen, S., Aragon-Salamanca, A., & Lahav, O. 1999, MNRAS, 303, 284
Rudnick, G., & Rix, H.-W. 1998, AJ, 116, 1163
Sandage, A. R. 1961, The Hubble Atlas of Galaxies (Publ. No. 618; Washington, DC: Carnegie Inst.)
Sandage, A. R., & Bedke, J. 1994, The Carnegie Atlas of Galaxies (Washington, DC: Carnegie Inst.).
Schade, D., Lilly, S. J., Crampton, D., Hammer, F., Le Fevre, O., & Tresse, L. 1995, ApJ, 451, L1
Schweizer, F. 1976a, ApJS, 31, 313
———. 1976b, ApJ, 168, 333
Serra-Ricart, M., Calbet, X., Garrido, L., & Gaitan, V. 1993, AJ, 106, 1685
Spiekermann, G. 1992, AJ, 103, 2102
Storrie-Lombardi, M. C., Lahav, O., Sodre, L., Jr., & Storrie-Lombardi, L. J. 1992, MNRAS, 259, 8
Tully, R. B. 1988, Nearby Galaxies Catalogue (Cambridge: Cambridge Univ. Press)
van den Bergh, S., Abraham, R. G., Ellis, R. S., Tanvir, N. R., Santiago, B. X., & Glazebrook, K. G. 1996, AJ, 112, 359
van den Bergh, S. 1960a, ApJ, 131, 215
———. 1960b, ApJ, 131, 558
Vorontsov-Velyaminov, B. A. 1977, A&AS, 28, 1
Watanabe, M., Kodaira, K., & Okamura, S. 1985, ApJ, 292, 72
Whitmore, B. .C. 1984, ApJ, 278, 61
Wu, K. L., Faber, S. M., & Lauer, T. 1997, BAAS, 191, 105.10
Zaritsky, D., Zabludoff, A. I., & Willick, J. A. 1995, AJ, 110, 1602